J. Fluid Mech. (1994), *vol.* 267, *pp.* 53–82

The life-cycle of tripoles in two-dimensional incompressible flows

By XAVIER CARTON† AND BERNARD LEGRAS‡

[1]SHOM/GRGS, 18 Av. Edouard Belin, 31055 Toulouse Cedex, France
[2]Laboratoire de Météorologie Dynamique du CNRS,
École Normale Supérieure, 24 rue Lhomond, 75231 Paris Cedex 05, France

(Received 4 June 1993, and in revised form 9 November 1993)

The mechanisms of coherent tripole formation from unstable shielded circular vortices are analysed in the context of two-dimensional incompressible flows. Three stages are identified during the transformation process: the linear growth of the initial normal mode perturbation, its nonlinear amplification and the finite-amplitude saturation under the tripolar form. We give a geometrical discussion of the mutual influence of the core vortex and of the satellites generated from the shield. The role of the angular momentum in determining the finite amplitude saturation is demonstrated using a simple elliptical model of the core vortex associated with two point-vortex satellites. The long-time asymmetric breaking of the tripole into a dipole and a monopole is shown to be driven by the erosion of the core vortex by stripping and diffusion. Finally the influence of bottom topography on tripole formation is considered, providing a rich phenomenology when the height of the topography is varied.

1. Introduction

In recent years, fine-scale studies of two-dimensional turbulence have borne out the primary contribution of long-lived coherent vortex structures to the dynamics of two-dimensional flows described, e.g., by the works of Basdevant *et al.* (1981) and McWilliams (1984). In most cases, the vortices are monopolar structures with a quasi-circular or elliptical shape transported and deformed by the velocity field due to other vortices. However, in a few but significant cases, the vorticity has been seen to condense into multipolar structures such as dipoles and tripoles (Legras, Santangelo & Benzi 1988).

The need immediately arises to determine the origin and the stability of these multipoles in isolation as well as in the presence of a large-scale deformation field. It has been demonstrated analytically (Flierl 1988) and numerically (Gent & McWilliams 1986) that the existence of an opposite-sign annulus around a circular vortex (hereafter dubbed 'shielded') may give birth to intense barotropic instability of azimuthal mode 2, leading to breaking into two dipoles. More recently, laboratory experiments (van Heijst, Kloosterziel & Williams 1991) and numerical simulations (Carton, Flierl & Polvani 1989; Orlandi & van Heijst 1992) have recorded many circumstances in which this process can nonlinearly stabilize to produce a stationary tripolar vortex with distributed vorticity. For their part, Polvani & Carton (1990) have exhibited the shapes of constant-vorticity tripolar steady states and numerically shown their robustness.

The present study gives a dual description and analysis of the transformation of a shielded monopole into a tripole: on the one hand, the flow is separated into the axisymmetric component and into the azimuthal deviation with their self and mutual interactions ; on the other hand, the vortex structure is decomposed into a core and a shield, later to form two satellites, the geometrical features and vorticity exchanges of which are detailed and quantified. The basic profile and the numerical methods are described in § 2.

The time evolution of the instability splits into three stages. First, the linear growth of the perturbation (§ 3) is characterized by an invariant structure of the eigenmode which folds the outer annulus and concentrates the peripheral vorticity into two side lobes. In the following stage (§ 4), the external poles exert a strain on the central region resulting in vorticity strands being pulled away from this latter and wrapped around the side lobes. This initiates a positive feedback loop which amplifies the instability. The radial shape of azimuthal mode 2 is altered, and harmonics are generated. Section 5 describes the saturation process during which the core vortex and the two external satellites align themselves. At the same time, the external strain decreases owing to the absorption within the satellites of opposite-sign vorticity strands, coming from the core vortex. The tripole has acquired its quasi-invariant rotating configuration with a nonlinear functional relation between vorticity and stream function. In § 6, an elliptical-vortex model is used to study under which circumstances the instability leads to breaking into two travelling dipoles instead of stabilizing as a tripolar structure. It is shown that the governing parameter is a conserved quantity, the angular momentum of the vortex.

A new phenomenon is presented in § 7: after a long life-span, the tripole is subjected to an asymmetric instability during which the core vortex and one satellite pair together while the other satellite remains isolated. This event is conjectured to stem from the instability of the vorticity ring which is built at the periphery of the tripole by repeated stripping of the core vortex. An analytical model with variable-strength point vortices is developed to reproduce this instability. The whole process is crucially dependent on how vorticity diffuses across the high-vorticity gradient which encircles the core vortex. Finally, we discuss in § 8 the influence of an axisymmetric topography on the tripole formation. Discussion and further conclusions are offered in § 9.

2. Model and initial conditions

We consider a two-dimensional incompressible barotropic flow in a $2\pi \times 2\pi$ bi-periodic domain. The governing vorticity equation is

$$\partial_t \zeta + J(\psi, \zeta) + J(\psi, \eta) = -(-1)^{n/2} \nu_n \nabla^n \zeta , \tag{2.1}$$

where $\zeta = \nabla^2 \psi$ is the vorticity, ψ the stream function, and $J(\ )$ is the two-dimensional Jacobian operator. The orography η vanishes except in § 8. Dissipation is provided by the right-hand-side hyper-viscosity operator which is a numerical device to get rid of the enstrophy carried towards small scales of motion. The value of ν_n is chosen in order to yield a dissipative range with exponentially decreasing spectrum as close as possible to the numerical cut-off.

This equation is discretized on a square grid with resolution $N_x = N_y$ equal to 128, 256 or 512. The spatial derivatives are exactly computed by Fourier transforms (using the well-known pseudo-spectral method) and the time advection is either a mixed Euler–leapfrog scheme or an Adams–Bashforth scheme. The time step is $\Delta t = 0.1$ for

a spatial increment $\Delta x = L_x/128$, and varies as $(\Delta x)^{-1}$ when the resolution increases according to the Courant–Friedrichs–Lewy stability condition. The hyper-viscosity has order $n = 4$ at resolutions 128^2 and 256^2, and order $n = 8$ at resolution 512^2. The dissipative coefficients are respectively $\nu_4 = 5 \times 10^{-8}$, $\nu_4 = 10^{-8}$ and $\nu_8 = 1.5 \times 10^{-18}$.

The initial flow consists in a perturbed axisymmetric vortex with zero total circulation. We choose the basic axisymmetric distribution among the family described by

$$\bar{\zeta}_\alpha = \left(1 - \frac{\alpha}{2} r^\alpha\right) \exp(-r^\alpha). \tag{2.2}$$

This vortex has a cyclonic core surrounded by an anticyclonic ring † and its amplitude decays exponentially for large r. By integrating $r\exp(-r^\alpha)$ by parts, using $(\mathrm{d}/\mathrm{d}r)\exp(-r^\alpha) = -\alpha r^{\alpha-1}\exp(-r^\alpha)$, one easily sees that the total circulation is zero for any α. Owing to these properties, the vortex has finite energy and angular momentum. The grid size $L_x = L_y = 2\pi$ is sufficient to consider a shielded vortex as isolated, since its total circulation vanishes rapidly with increasing r. By linearizing (2.1) (with $\eta = R = \nu = 0$) near $\bar{\zeta}_\alpha$, we get the Rayleigh problem which has been studied by Carton *et al.* (1989). We choose as initial perturbation to the basic profile $\bar{\zeta}_\alpha$ the most unstable eigenvector of the Rayleigh problem which is of the form

$$\zeta'(r,\theta) = \mathrm{Re}\,[Z(r)\,\mathrm{e}^{\mathrm{i}\ell\theta}]. \tag{2.3}$$

This initialization has a robust physical basis: if instead of a normal mode, we use a small-amplitude white-noise initial perturbation, the pattern of the most unstable mode soon dominates the growing perturbation (Orlandi & van Heijst 1992). The calculation of the eigenmodes is numerically achieved with IMSL routine EIGZF, with enough nodes in the radial direction to match the asymptotic solution of Gent & McWilliams (1986) at large r (i.e. $\psi' \sim \mathrm{Re}[r^{-\ell}\, e^{i\ell\theta}]$) which is used as boundary condition.

Carton *et al.* (1989) found that the profile $\bar{\zeta}_\alpha$ becomes unstable for $\alpha > 1.85$ and perturbations with azimuthal wavenumber $\ell = 2$. They showed that $\ell = 2$ is the most unstable wavenumber for $\alpha < 6.0$. In the tank experiment of van Heijst *et al.* (1991), the core of the initial vortex apparently follows a Gaussian profile for the stream function (i.e. it satisfies (2.2) with $\alpha = 2$) but their data are not accurate enough to determine the aisle of the profile which is a crucial paramater as we shall see below. Orlandi & van Heijst (1992) found that the instability of the profile $\bar{\zeta}_2$ leads to a tripole somewhat less elongated than that observed in tank experiments. As in Carton *et al.* (1989) we choose instead to focus here on the case $\alpha = 3$ which seems more representative of tripole dynamics and also produces patterns that closely resemble the tripoles in a laboratory rotating tank. The e-folding time of the most unstable mode is then $\tau = 13.03$.

The maximum amplitude of the perturbation stream function is 0.001 for the experiments in 128^2 and 256^2 and 0.01 for the experiment in 512^2, corresponding respectively to 0.015 and 0.15 for the maximum amplitude of the vorticity perturbation of the basic profile $\bar{\zeta}_3$. The two lower-resolution experiments start at $t = 0$. Owing to its stronger initial perturbation, the high-resolution experiment is considered to start at $t = 30$.

Figure 1 shows a series of vorticity charts taken during the evolution of the vortex from the perturbed axisymmetric structure to a well-developed tripole by the end

† Here cyclonic means anticlockwise rotation while anticyclonic means clockwise rotation, a situation arising on a rotating device with positive angular velocity

of the experiment. The following sections discuss the three stages of this evolution: linear stage, nonlinear amplification and nonlinear saturation.

3. Linear instability

If the amplitude of the initial perturbation is chosen of the order of one-hundredth of that of the basic axisymmetric profile, the first stage of the evolution is linear. Figure 2 shows the vorticity distribution of the most unstable mode obtained from the resolution of the Rayleigh equation with a basic profile $\bar{\zeta} = \bar{\zeta}_3$. The zero amplitude line of the perturbation closely corresponds to vanishing $\partial\bar{\zeta}/\partial r$, i.e. to maximal anticyclonic mean shear in the outer region, while the perturbation reaches maximum amplitude near the zero vorticity line of the basic profile. An anticlockwise shift of the four external poles with respect to the internal ones is required, as we shall see shortly, to satisfy the instability condition.

These features are the axisymmetric analogues of the properties of unstable modes for parallel flows seen from the point of view of vorticity dynamics (Hoskins, McIntyre & Robertson 1985, see also Flierl 1988). Here, each positive (respectively negative) pole induces a cyclonic (resp. anticyclonic) circulation in its vicinity. Thus the phase shift is such that each internal positive (resp. negative) pole is submitted to an outward (resp. inward) flow induced by the external poles. This motion reinforces both the internal and external poles which are immersed within a region of negative (resp. positive) outward gradient of the mean vorticity profile. The effect is maximum when the external and internal poles are in quadrature. In addition, the coupling between internal and external poles induces a differential angular rotation which goes against the natural tendency of the two systems to rotate in opposite directions. The effect is then maximum when the internal and external poles are in phase. This is the situation at critical α when the growth rate is marginal. For supercritical values of α, the poles of the unstable eigenmode are located such that the differential rotation rate vanishes and the perturbation amplifies. The fact that the external poles of the perturbation are entirely contained within the region of positive vorticity gradient shows how important the knowledge of the aisle of the basic profile is to determine its stability properties.

When α increases from its critical value, it can be shown (see Carton 1988) that the most unstable mode has its peak amplitude at decreasing radii, from $r = 1.2$ for $\alpha = 2.0$ down to $r = 0.8$ for $\alpha = 4.0$, while the phase shift between internal and external poles increases from $\delta\phi = 0.2$ to $\delta\phi = 1.0$. This is in agreement with the inward displacement of the maximum jet located at $r = r_1 \equiv (1/\alpha)^{1/\alpha}$ with value $U_{max} = \frac{1}{2}(e\alpha)^{-1/\alpha}$ and of the maximum anticyclonic shear located at $r = r_2 \equiv (1 + 1/\alpha)^{1/\alpha}$ with value $A_{max} = -\frac{1}{2}e^{-(1+1/\alpha)}$.

The stability properties are thus related to the increase of the maximum shear with α. Notice also that the steepness of the vorticity profile $\bar{\zeta}_\alpha$ can be measured, for instance, by its slope where the basic profile vanishes, that is $-\frac{1}{2}\alpha^2 e^{-2/\alpha}$. Since this quantity increases in absolute value as α increases, we see that the separation between the core and the exterior ring decreases. As a result, the coupling between the internal and the external perturbations of vorticity contours is an increasing function of α. For subcritical values of α, the phase locking between the external and the internal perturbations cannot be maintained, thus the vortex is stable.

A simple model of tripolar instability can be obtained by considering an initial axisymmetric vortex with piecewise uniform vorticity in four concentric regions: $q = q_0$ for $0 < r < a$, $q = q_1 = -q_0 a^2/(c^2 - b^2)$ for $b < r < c$, with $a < b$, and zero

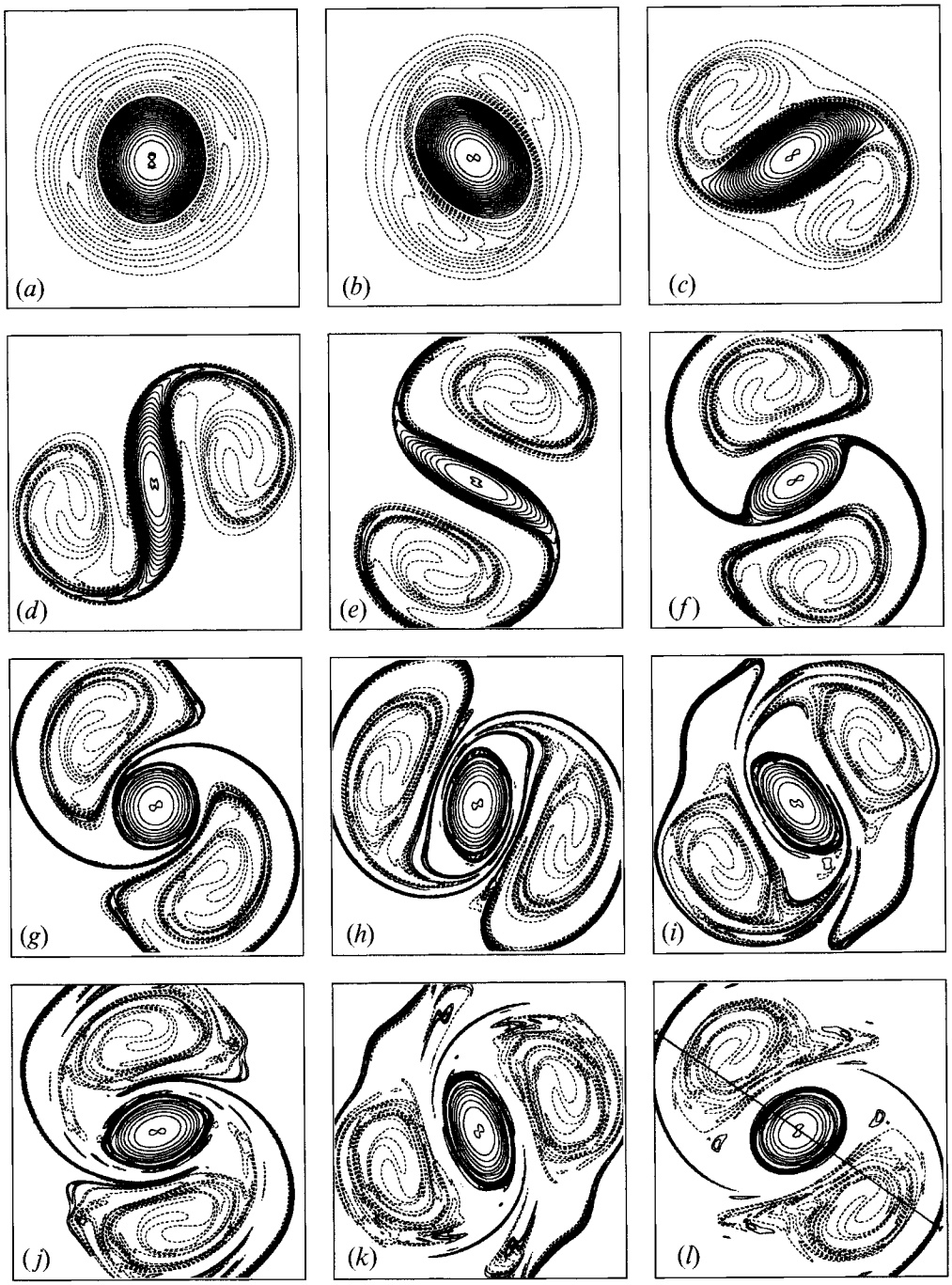

FIGURE 1. Vorticity maps from the 512^2 experiment at various times. Contour interval 0.05. Solid contours for positive vorticity and dashed contours for negative vorticity. The frame is centered and shows $\frac{11}{16} \times \frac{11}{16}$ of the periodic $2\pi \times 2\pi$ box. (*a*) $t = 30$ (2.3τ); (*b*) $t = 40$ (3.07τ); (*c*) $t = 55$ (4.22τ); (*d*) $t = 70$ (5.37τ); (*e*) $t = 85$ (6.52τ); (*f*) $t = 100$ (7.67τ); (*g*) $t = 107$ (8.21τ); (*h*) $t = 120$ (9.21τ); (*i*) $t = 140$ (10.74τ); (*j*) $t = 160$ (12.28τ); (*k*) $t = 195$ (14.97τ) and (*l*) $t = 230$ (17.65τ). Figure 8 shows the vorticity profile along the section.

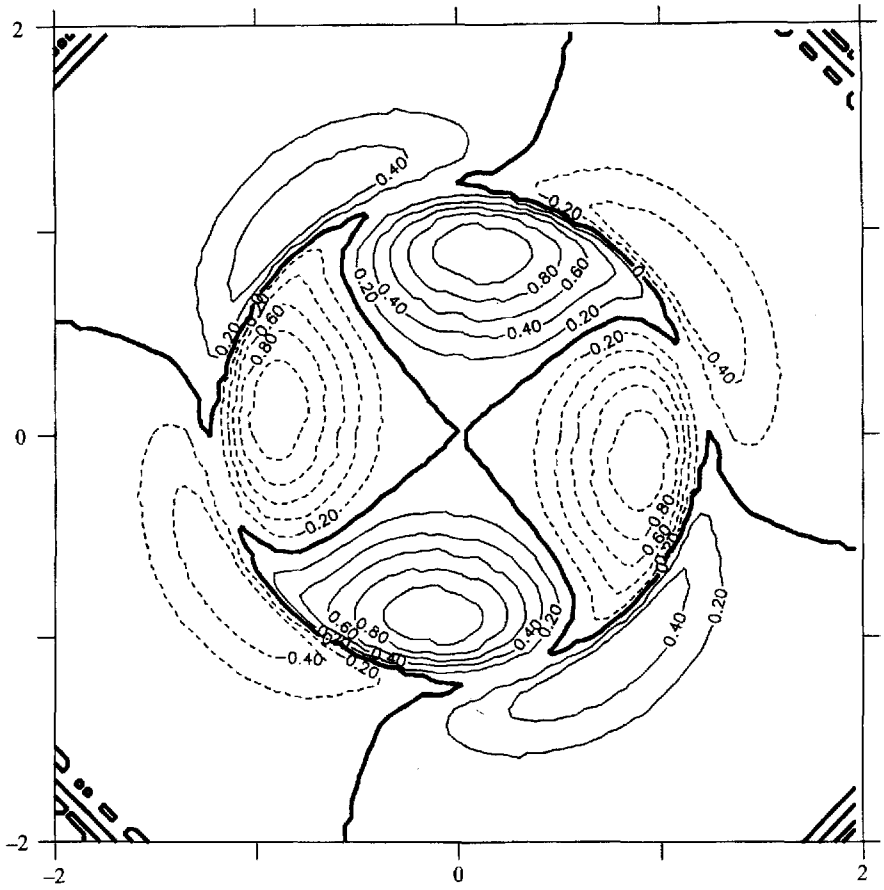

FIGURE 2. Vorticity distribution of the most unstable mode for the basic profile $\bar{\zeta} = \bar{\zeta}_3$ and $\ell = 2$. The amplitude is arbitrary.

vorticity in the annulus $a < r < b$ and the exterior region $r > c$. This vortex has zero total circulation and a radial velocity profile $V(r)$ given in (A 1). For $a = b$, it is known (Flierl 1988) that this profile is unstable to azimuthal wavenumber $\ell = 2$ perturbation for $\frac{1}{2}c < a < c$. This instability does not saturate as a tripole but yields a pair of dipoles. The calculation of the characteristic equation for the more general case $a \leqslant b$ is given in Appendix A. Figure 3 shows the resulting stability diagram in the $(a/c, b/c)$-plane.

A quantitative comparison with the profile $\bar{\zeta}_\alpha$ is possible by fitting the relevant characters of the discrete and the continuous profiles. By requiring that the two profiles have the same maximum velocity at the same position, we obtain the two relations $a = (1/\alpha)^{1/\alpha}$ and $q_0 = \mathrm{e}^{-1/\alpha}$. By further imposing the same vorticity where the shear is maximum, we obtain $q_1 = -\frac{1}{2}(\alpha - 1)\mathrm{e}^{-(1+1/\alpha)}$. The boundaries b and c of the external annulus are then determined by requiring equal angular momentum, giving $2\int_0^\infty r^3 \bar{\zeta}_\alpha(r) = q_0 a^4 - q_1(c^4 - b^4)$, and zero total circulation, giving $q_1(c^2 - b^2) = q_0 a^2$. Finally, by rescaling a and b by c, we obtain a curve $(a/c, b/c)$ as a function of α which is appended to the stability diagram on figure 3. It turns out that this curve intersects the stability boundary for $\alpha = 1.65$, within less than 11% of the true critical

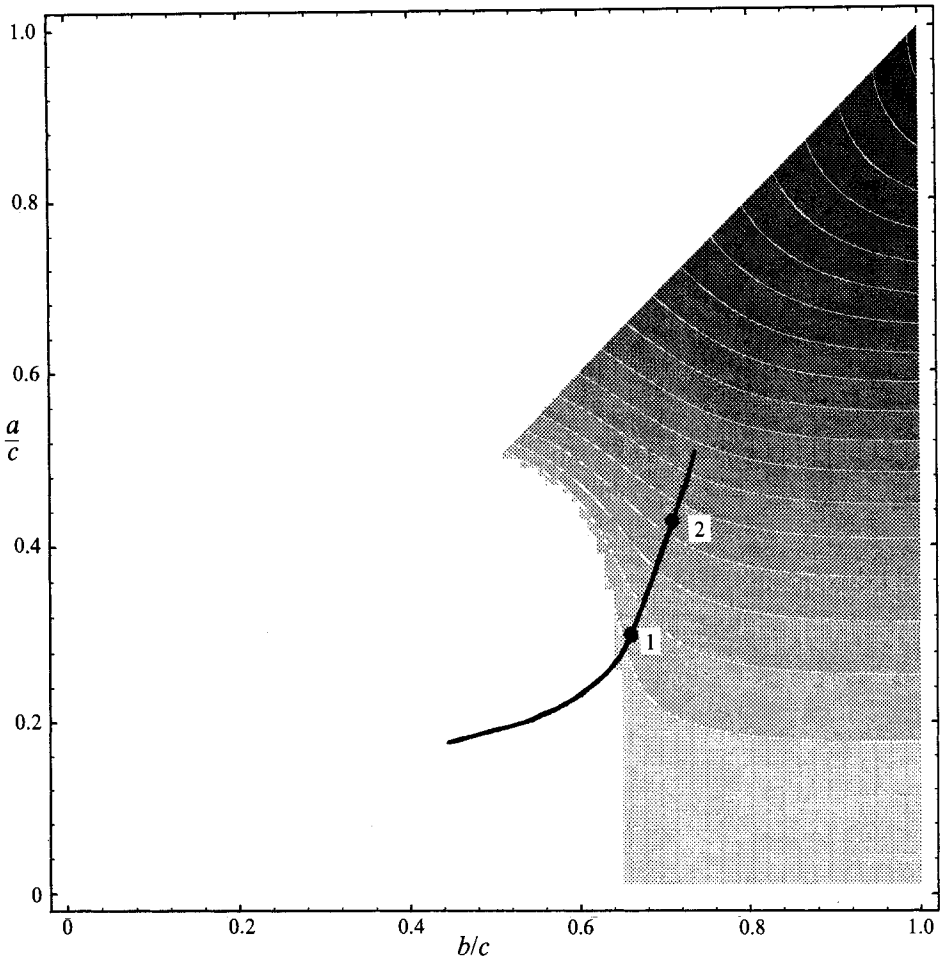

FIGURE 3. Value of $\hat{c}_i$, the imaginary part of $\hat{c}$, obtained by solving (A 3), for $0 < a < b < c$. The $\ell = 2$ perturbation is neutral within the blank region under the diagonal. The solid-line curve fits the vorticity profile $\bar{\zeta}_\alpha$ within the $(a/c,\ b/c)$-plane, see text, for $1.2 < \alpha < 4$. Points marked 1 and 2 show respectively the location of $\alpha = 1.85$ (critical value) and $\alpha = 3$.

value, a striking result considering the crudness of our approximation which suggests that the instability is characterized by only a few global measures of the flow.

Figure 4 shows, on a log-linear scale, the evolution of the amplitude of the dominating azimuthal modes at the intermediate resolution 256^2. Here the modes are defined irrespective of the solution of the Rayleigh problem. For any azimuthal wavenumber ℓ, we have

$$\{C_\ell(r),\ S_\ell(r)\} = \frac{1}{\pi}\int_0^{2\pi} \psi'(r,\theta)\{\cos\ell\theta,\ \sin\ell\theta\}\,\mathrm{d}\theta,$$

and

$$\bar{A}_\ell = \frac{1}{r_{max}}\int_0^{r_{max}} \left[C_\ell^2(r) + S_\ell^2(r) r\,\mathrm{d}r\right]^{\frac{1}{2}},$$

with $r_{max} = \pi$. It is apparent that the period of exponential growth of the most

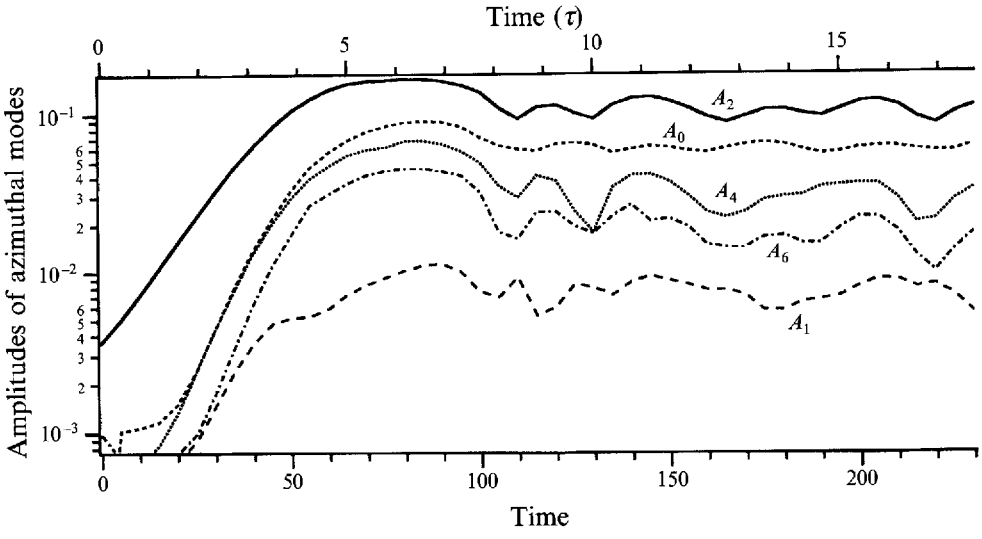

FIGURE 4. Evolution of the main components of the azimuthal mode decomposition of the perturbation. See definition of the amplitude $\bar{A}_\ell$ in the text.

unstable mode $\ell = 2$ lasts up to $t \approx 3\tau$. During this period, we observe that the perturbation simply grows in amplitude without changing shape. The vorticity distribution at $t = 3.07\tau$ is shown in figure 1(*b*). The measured e-folding time of mode $\ell = 2$ between $t = 0$ and $t = \tau$ is slightly smaller, by 6 %, than the theoretical linear value τ. Nonlinearities are inducing the development of other harmonics: modes $\ell = 0, 4, 6$ grow with an e-folding time of 0.7τ and at $t = 3\tau$ the first two reach an amplitude ratio 1:4.5 with the main mode. Mode $\ell = 1$ and other odd modes (not shown) grow out from numerical noise but remain of very weak amplitude. There seems to be very little feedback effect onto mode $\ell = 2$ during this stage. This is further confirmed by the fact that the high-resolution experiment (in 512^2) which begins at time $t = 2.3\tau$ with a purely linear perturbation closely follows the evolution of the other two, as is shown below.

4. Nonlinear amplification

From $t = 3\tau$ to 5.5τ (see figure 1*c*, *d*), the perturbation amplifies in the outer region where it generates two well-defined anticyclonic satellites while the cyclonic core progressively becomes more elongated. A detailed visual inspection reveals that the two satellites are growing by entrainment and wrapping of the exterior anticyclonic vorticity around the two outer centres which have emerged from the linear instability. Each of these two centres induces around itself an anticyclonic flow which decreases with distance. Hence, the cyclonic core vortex is submitted to a strain field the dilation axis of which is rotated by 45° with respect to the line joining the satellite centres. It is known (Kida 1981) that a top-hat vortex undergoes strong vacillations when it is abruptly submitted to a strain. On the contrary, we observe here that the core evolves in a monotonic way with very weak phase vacillations and stays close to the instantaneous equilibrium position which would imply exact alignment of its small axis with the satellites. Such a quasi-adiabatic evolution is often observed for

distributed vortices. This effect has been recently analysed by Legras & Dritschel (1993*b*) in the case of a slowly growing shear.

The total strain felt by the core vortex combines an internal contribution γ_i due to the elongation of the core and an external contribution γ_e due to the satellites. We can separate these two components by using the method described in Appendix B. Figure 5 shows γ_i and γ_e as a function of time for the high-resolution experiment. The internal strain undergoes large variations which are perfectly correlated with the vacillations of the aspect ratio of the core vortex. The external strain displays a quiescent evolution, growing until $t \approx 5.5\tau$ and slightly decaying later on towards a quasi-stationary regime with superimposed oscillations. Although the external strain is smaller than the internal strain, it is solely this component which is able to change the aspect ratio of the core vortex, since the internal contribution can only induce rotation. The maximum value of the external strain is, indeed, about 75% of what is necessary to completely tear out the core vortex. However, the variations of the aspect ratio also depend on the angle $\Delta\phi$ between the core vortex and the external strain. The relevant quantity is $\gamma_f = \gamma_e \sin 2\Delta\phi$: the aspect ratio increases when γ_f is positive and decreases when it is negative (Legras & Dritschel 1991). Figure 5 shows that the estimated γ_f is, indeed, closely correlated with the temporal derivative of the measured aspect ratio for $t > 8\tau$. The lack of agreement near the first maximum of the aspect ratio is due to the fact that our diagnostics only considers the strain at the centre of the vortex while a very elongated core may be submitted to significant variations of the strain along its major axis.

In turn, the rotation of the core vortex depends on the sum of its own contribution and that due to the external strain. Under the approximation of a uniform aspect ratio, the former can be estimated as $\Omega_i = \omega_0\lambda/(1+\lambda^2)$ while the latter is $\Omega_e = -\gamma_s(1-\lambda^2)/(1+\lambda^2)\cos 2(\phi-\phi_s)$. These two opposite tendencies are shown in figure 6 where their sum is compared to the observed rotation of the core vortex $\Omega(t)$. Our approximation tends to slightly overestimate the rotation rate and there are also spurious oscillations during the linear stage. We see that both internal and external components decrease in absolute value as the aspect ratio increases from $t = 0$ to $t = 6.7\tau$ but their sum only varies weakly. Since the rotation of the satellite also decreases when the aspect ratio of the core increases (see § 6), the core rotates faster than the satellites. At $t = 6.7\tau$, the main axis of the core is orthogonal to the satellites and the aspect ratio reaches a maximum. It can be seen from figure 2 that all the perturbation modes reach their maximum amplitude at this time.

Within a framework rotating with the core vortex the instantaneous stream function, shown in figure 7 at $t = 5\tau$, exhibits two critical saddle-points where the velocity vanishes. Two pairs of separatrices emanate from these points isolating a centre region, which basically corresponds to the core, from the two lobes containing the satellites. As the instability develops, the motion of the critical points is governed by two opposite tendencies: an inward motion directly due to the increasing external strain and an outward motion due to the increasing elongation of the core. Indeed, it is observed for $\alpha = 3$ that the location of the critical points varies weakly during the generation of the tripole, staying at distance $r = 1.2(\pm 3\%)$ from the centre. Since the core is rapidly elongating under the action of the external strain, new vorticity contours of the core are continuously crossing the saddle-points. Hence, vorticity strands are entrained within the satellites where they wrap at increasing distance from the centre as time proceeds. The spiral structure which is visible in rotating tank experiments (van Heijst *et al.* 1991) or in our numerical experiment (see figure 1 and figure 8) is a direct consequence of this dynamics.

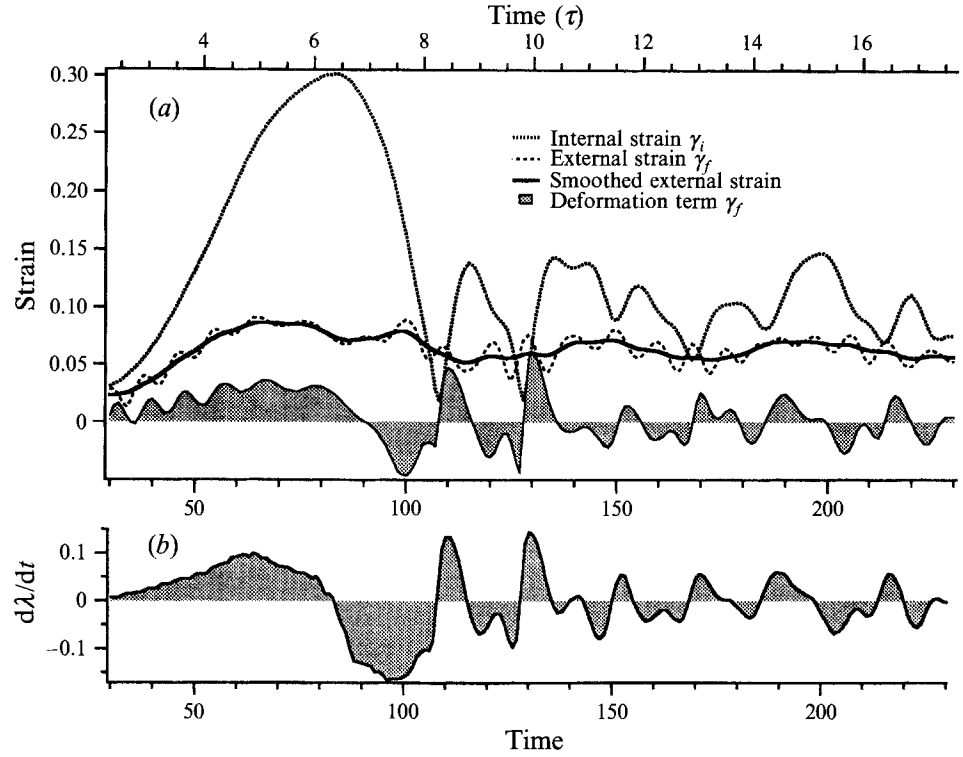

FIGURE 5. (*a*) Internal and external strain, and deformation term as a function of time. (*b*) Time derivative of the aspect ratio for vorticity contour $\zeta = 0.6$. See text for definitions.

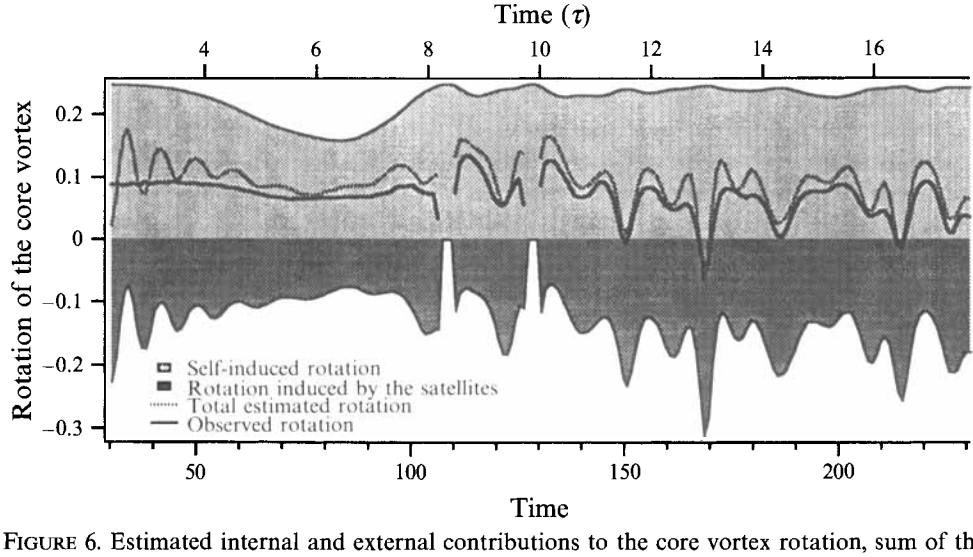

FIGURE 6. Estimated internal and external contributions to the core vortex rotation, sum of the two and observed rotation. Overturning episodes are eliminated.

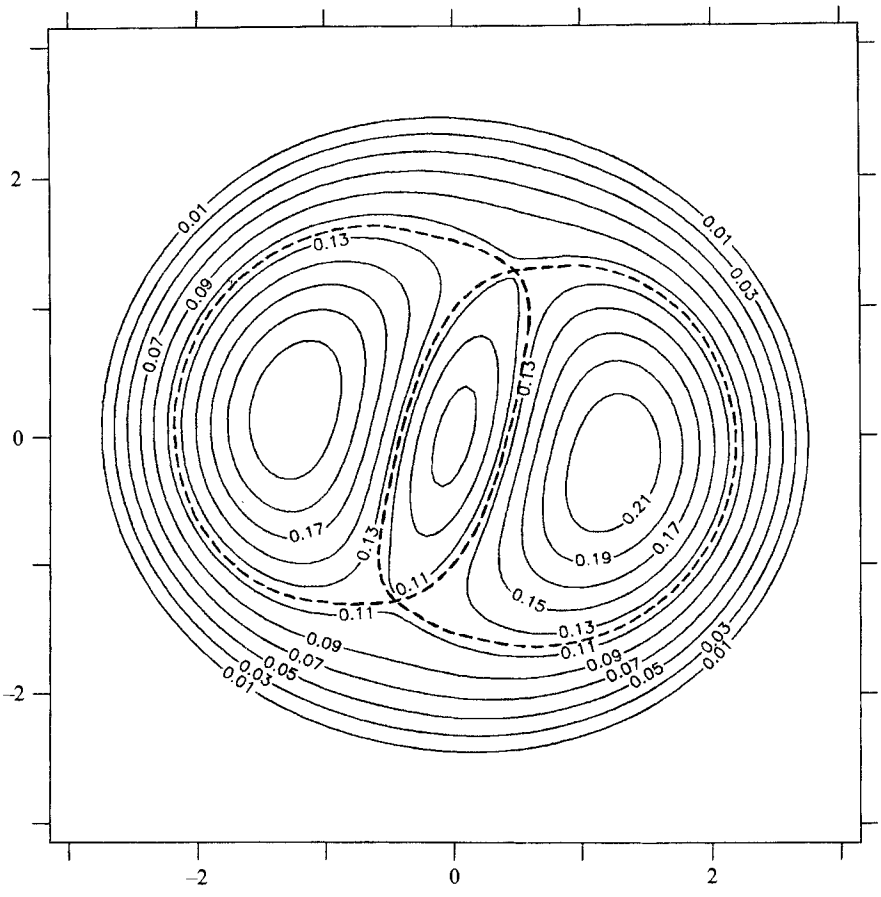

FIGURE 7. Stream function at $t = 5.37\tau$ in a framework rotating with angular velocity $\Omega = 0.0715$. The separatrices which cross at the two saddle points are shown by dashed lines.

By entraining more anticyclonic vorticity, the satellites grow in intensity and, consequently, the strain also increases over the central region (see figure 5) completing the positive feedback loop which causes the nonlinear amplification of the tripole.

The existence of saddle-points linked by separatrices (see figure 7) is known in the literature on dynamical systems to be a structurally unstable situation which leads to chaotic trajectories when an external perturbation (even periodic) is applied (see e.g. Beigie, Leonard & Wiggins 1992). Since vorticity is entrained along the separatrices, we may wonder why we get a stable pattern instead of chaos. The reason lies in the outward motion of the external separatrices. As the core gets more elongated, the two lateral lobes also increase in size; the vorticity initially located near the separatrices can therefore be entrained into the lobe where it forms the spiral mentioned above. During this stage, no vorticity is reinjected in the vicinity of the saddle-points, no amplification of the fluctuations can take place and the evolution remains predictable.

5. Finite-amplitude saturation

After $t = 6.7\tau$ (see figure 1*e*) the aspect ratio of the core vortex decreases abruptly. The underlying mechanism is that decreasing the aspect ratio induces an increase of

the angular rotation of the core vortex which, if it is not compensated by the faster rotation of the satellites, leads to further decrease of the aspect ratio. Indeed, we observe here that the rotation of the core vortex accelerates and that at $t = 8.3\tau$ (see figure 1*g* and figure 9) the core undergoes a complete turning-over. A similar event occurs at $t = 9.8\tau$ after the core has again passed through the orthogonal position to the satellites at $t = 8.8\tau$. We see that the second maximum of the aspect ratio (or equivalently γ_i) is much weaker than the first one. These two complete rotations of the core are followed by oscillations, with average period $T = 2.2\tau$, during which the core vacillates around an apparent equilibrium position with the satellites.

The vacillations of the core vortex bear strong similarities with the oscillations of an ellipse immersed within an external uniformly rotating strain field (Kida 1981) and initially released out of its equilibrium position. There are, however, noticeable differences in the fact that the rotation of the strain field (i.e. of the satellite) is here modulated by the aspect ratio and the orientation of the core and that the intensity also depends on the amount of material which has crossed the critical points and has been absorbed in the satellites.

In this respect, we observe that as early as $t \approx 4.2\tau$ (see figure 1*c*) the critical points cross the zero vorticity line. Henceforth, positive vorticity is expelled from the core vortex, forming two streamers around the two satellites near the exterior separatrices. This absorption of positive vorticity within the two satellites reduces their total circulation in absolute value and in turn reduces the external strain on the core vortex. It takes, however, some time for the two positive streamers to develop and the feedback effect onto the core is not immediately felt. We see on figure 5 that the external strain increases until $t = 5\tau$ and then decreases while the core reaches its maximum elongation. Assuming that the core then overshoots its equilibrium position with the external strain, the simultaneous decrease of this latter drives the core even further away from equilibrium and induces the observed fast tumbling.

While the core undergoes a fast evolution, the two satellites do not exhibit any significant variations of their central regions which evolve under a slow internal motion. Their periphery is, however, rapidly changing. It is difficult to define a rotating framework for the whole system but one can treat the satellites and the core vortex separately. The location of the critical points within the framework rotating with the core vortex is visualized by the points where the filaments are attached to the core vortex. The critical points within the framework rotating with the satellites are less easily identified. Their fluctuations allow an exchange of fluid between the two satellites as is clearly seen on figure 1(*i*) around $t \approx 11\tau$. This exchange mainly consists in streamers of positive vorticity which are lying near the external separatrices. Notice that after $t = 12.5\tau$ (see figure 1*j*) a part is recaptured by the core vortex. As the positive streamers travel around the tripole, the external strain on the core vortex varies accordingly. It has a maximum at $t = 11\tau$ when the streamers and the satellites, located at right angles, add their contribution and a minimum at $t = 13\tau$ when, being aligned, they act in opposite way.

We see from figure 1 that following the production of the two external cyclonic streamers, many vorticity contours are crowding at the periphery of the core vortex. The generation of high vorticity gradient is, indeed, a basic consequence of stripping (Legras & Dritschel 1993*a*, *b*). Figure 8 shows a cross-section of the vorticity field at $t = 230$, as indicated in figure 1(*l*), and compares it to the initial profile $\bar{\zeta}_3$. The sharp boundary of the core vortex produced by stripping is surrounded by a small region of low vorticity, corresponding to fluid particles entrained from outside. The satellite possess a complicated 'hairy' structure which is the trace of the wrapping of

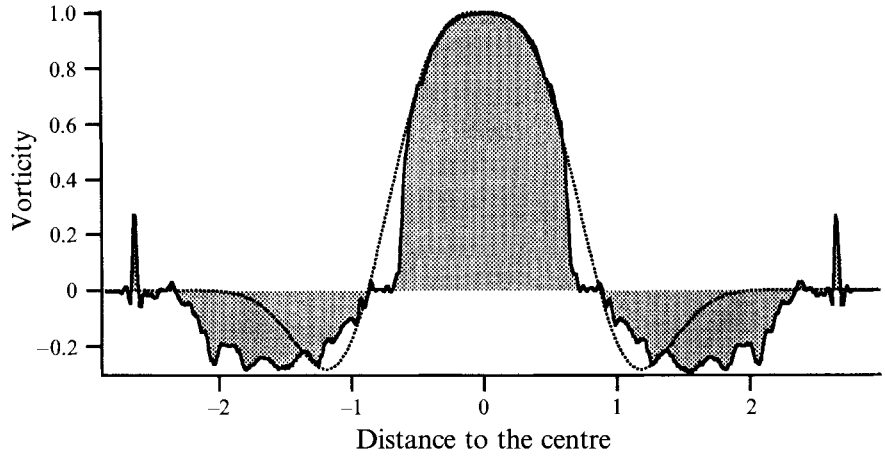

FIGURE 8. Solid line: cross-section of the tripole at $t = 230$ (indicated in figure 1*l*). Dotted line: initial profile $\bar{\zeta}_3$ magnified by a factor 1.09 along the abscissa to account for the elliptical deformation of the vortex core.

the vorticity streamers during their generation. The positive streamers are visible as the peaks of vorticity in the two aisles of the distribution. A second zone of entrained external fluid lies between them and the satellites.

The repeated stretching and folding of vorticity filaments when they pass near the perturbed critical points is the source of a complex dynamical behaviour (see Legras & Dritschel 1993*a*) which exhibits sensitivity to initial conditions and induces loss of predictibility. By comparing in figure 9 the aspect ratio for the two experiments in 256^2 and 512^2, we see that they stay very close during the development stages of the tripole, even if the initial conditions of the two experiments differ (see § 2). However, as time proceeds, the two curves show similar behaviour but they separate up to the point, by the end of the record, where oscillations of the core vortex occur in opposite phase in the two experiments. The main difference between the two experiments being the smoothing of small-scale chaotic filaments and high vorticity gradients which is stronger at low resolution, it is reasonable to see these structures as the cause of the diverging evolutions. Figure 9 shows, nevertheless, that the global dynamics of the tripole measured here by the rotation rate is rather insensitive to the resolution.

At later times, for $t > 18\tau$, which have only been explored with resolutions 256^2 and 128^2, the complicated filamentary structure is smoothed by dissipation. The tripole exhibits an apparently stable pattern with superimposed damped oscillations, which are visible in figure 10 for the aspect ratio of the core between $t = 18\tau$ and $t = 76\tau$. However, it will be shown in § 7 that the oscillations do not really damp to zero and that a new instability develops breaking the symmetry of the tripole. Hence, the symmetric tripole can only be considered as metastable for our initial condition and our value of the dissipation.

We may wonder whether a truly stationary solution does exist in the vicinity. In order to filter out the oscillations, we average the vorticity between $t = 17\tau$ and $t = 67\tau$ within a framework rotating at the mean angular velocity Ω of the tripole. Based on the observed rotation of the core vortex, we obtain $\Omega = 0.057$. The average vorticity in the rotating framework, shown in figure 11, exhibits a smooth pattern without any filamentary structures. In figure 12 we plot the stream function versus

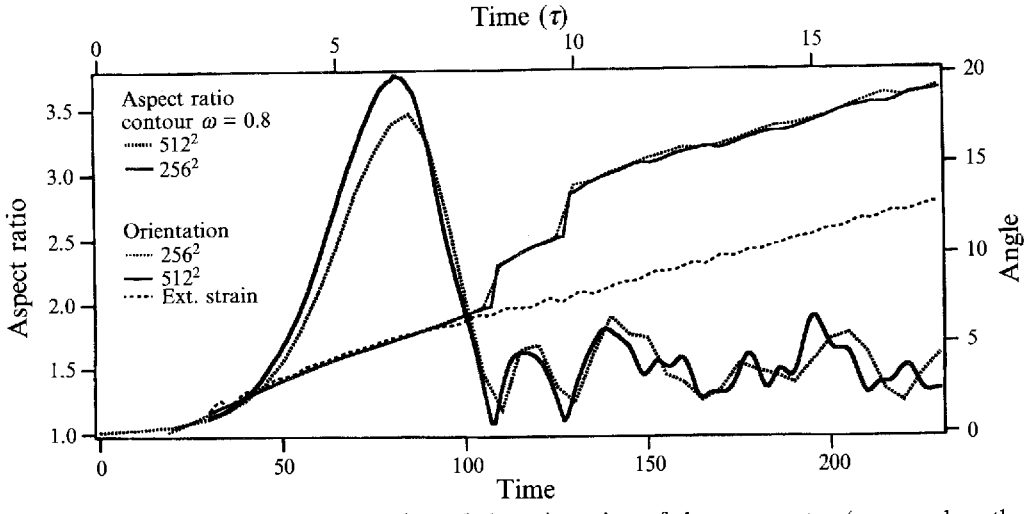

FIGURE 9. Evolution of the aspect ratio and the orientation of the core vortex (measured as the orientation of vorticity contour $\zeta = 0.8$) for the two experiments in 256^2 and 512^2. The angle calculated for the former has been shifted by -2.78. The orientation of the external strain in 512^2 is also shown.

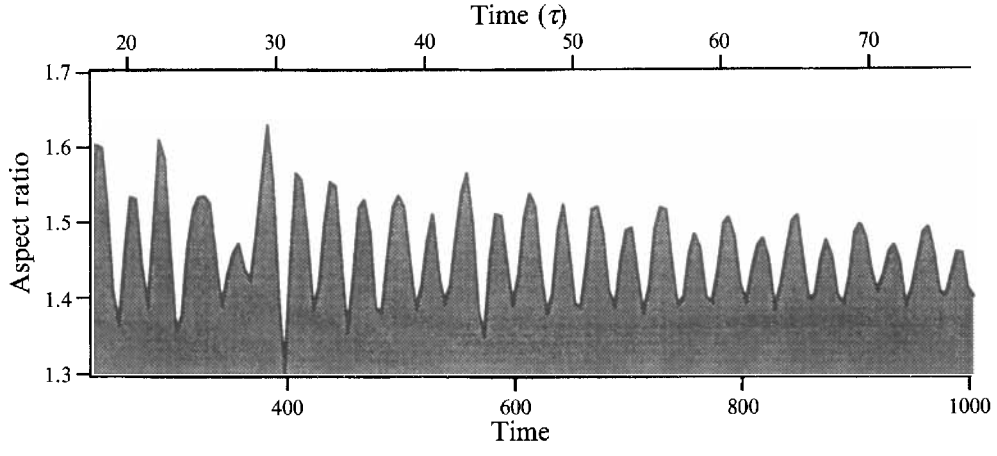

FIGURE 10. Aspect ratio of the vorticity contour $\zeta = 0.8$ between $t = 18\tau$ and $t = 76\tau$ for the intermediate resolution 256^2.

the vorticity in the rotating framework. The well-defined functional relationship demonstrates the stationarity of the average flow. This function is not linear but presents a curvy shape for both the core (positive value of ζ) and the satellites. It does not satisfy the prediction of Montgomery & Joyce (1974) that $\zeta(\psi)$ must have a curvature of opposite sign to ζ but is compatible with the family of relations arising from the statistical theory of Robert & Sommeria (1991). It is likely, however, that the high mixing which is a prerequisite for the application of statistical arguments is not effective here, especially within the core vortex which has only experienced adiabatic transformations without modifying its mean profile. The function also differs from

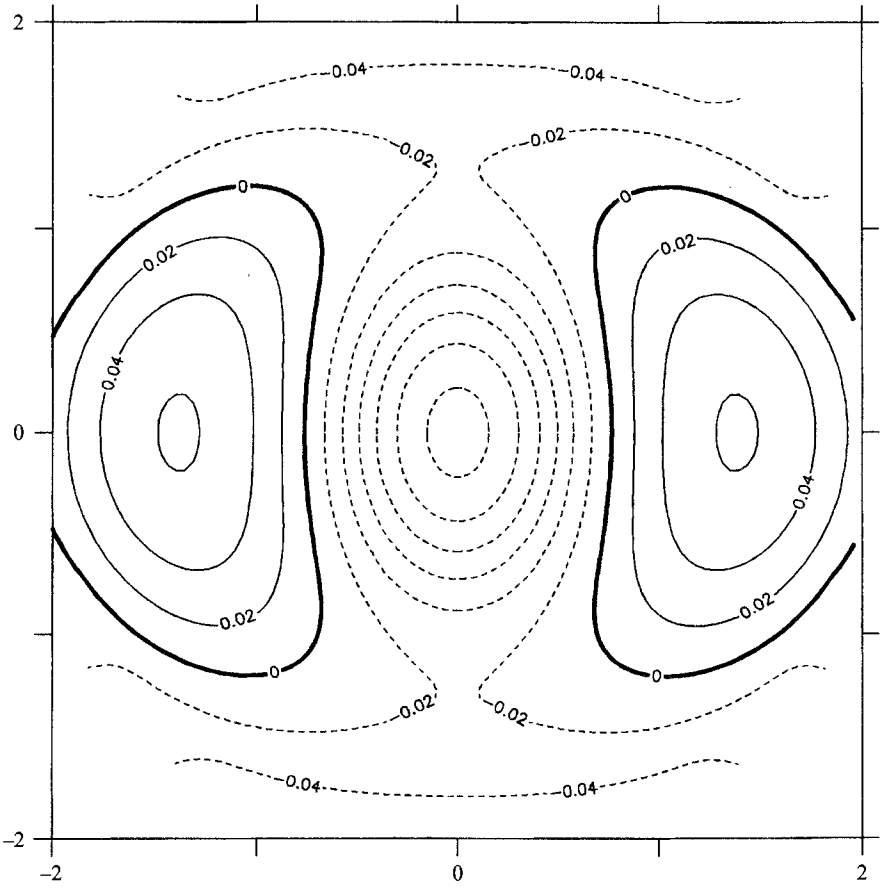

FIGURE 11. The stream function in the rotating framework with angular velocity $\Omega = 0.057$ averaged over the period $17\tau < t < 67\tau$.

that obtained by Orlandi & van Heijst (1992) with $\alpha = 2$. Notice finally that the stationary average solution may still be sensitive to the type of viscous instability described in § 7.

We have emphasized in this section the role of positive vorticity intruding into the anticyclonic satellites during saturation. For values of α closer to criticality, saturation of the tripolar instability occurs without this intrusion. Figure 13 shows one sequence of views extracted from one experiment with $\alpha = 2.5$ (see also figure 4 of Orlandi & van Heijst 1992, for the case $\alpha = 2$). Here the two satellites are entirely formed from the ring of negative vorticity and the instability saturates smoothly when the core gets to its maximum elongation. It can be shown that the separatrices of the stream function in the rotating frame are intersecting the satellites. Thus, exchanges of negative vorticity between the satellites occur after saturation of the instability, carrying strands of negative vorticity around the critical points. As a consequence, the distribution of negative vorticity becomes more axisymmetric, the external strain exerted on the core vortex decreases and the critical points move slightly away. As the exchange proceeds to its end, the two satellites separate again, reinforcing the strain. This is followed by a new intersection of the satellites with the lobes, initiating

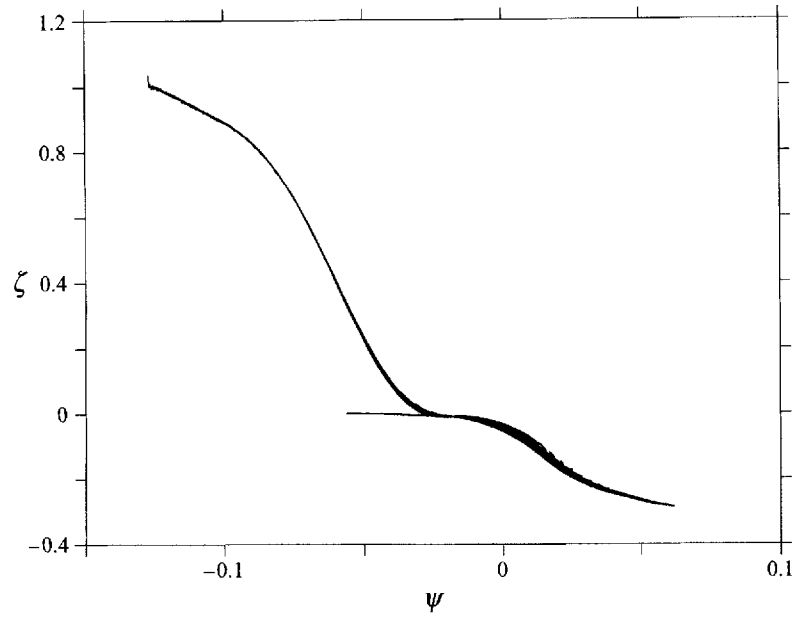

FIGURE 12. Vorticity versus stream function scatter plot for the averaged flow in the rotating framework.

a new oscillation. Unlike the case $\alpha = 3$, the elongation of the core vortex closely follows the variations of the external strain at any time.

For $\alpha \geqslant 3.2$, the instability does not saturate as a tripole but the core vortex breaks in two separate components which both form a pair with one of the satellites. The two resulting dipoles escape in two opposite directions. The vorticity patterns during and after breaking are very close to those shown in figure 19(*b*, *c*) where breaking is induced by topographic effects.

6. A simple model

Although the dynamics of the tripole exhibits a tremendous complexity, some of the basic features can be understood with very simple models. The maximum simplification is obtained (cf. van Heijst *et al.* 1991) by replacing the tripole by three point vortices with circulation Γ_c for the core and Γ_s for the two satellites. In the symmetric situation where the three vortices are aligned, the two satellites being located at distance a on both side of the core, the structure rotates steadily with angular velocity $\Omega = (2\Gamma_c + \Gamma_s)/8\pi a^2$. The separation a depends on the excess angular momentum $\mathscr{I} = 2a^2\Gamma_s$. As long as $\Gamma_c/\Gamma_s < -5/4$, it can be shown that the tripole is nonlinearly stable (for a thorough discussion of the dynamics of three point vortices, see Tavantzis & Ting 1988). Symmetric oscillations of the satellites around the equilibrium position occur with frequencies $\mu_{\pm} = \pm[-3\Gamma_s(2\Gamma_c + \Gamma_s)/8\pi^2 a^4]^{\frac{1}{2}}$. Notice that for the case of vanishing total circulation, $\Gamma_s = -\frac{1}{2}\Gamma_c$, one of the two frequencies coincides with the angular rotation. According to van Heijst *et al.* (1991) the angular velocity deduced from the model is 25% greater than the measured value in rotating tank.

The point-vortex model is, however, unable to explain why, depending on the initial

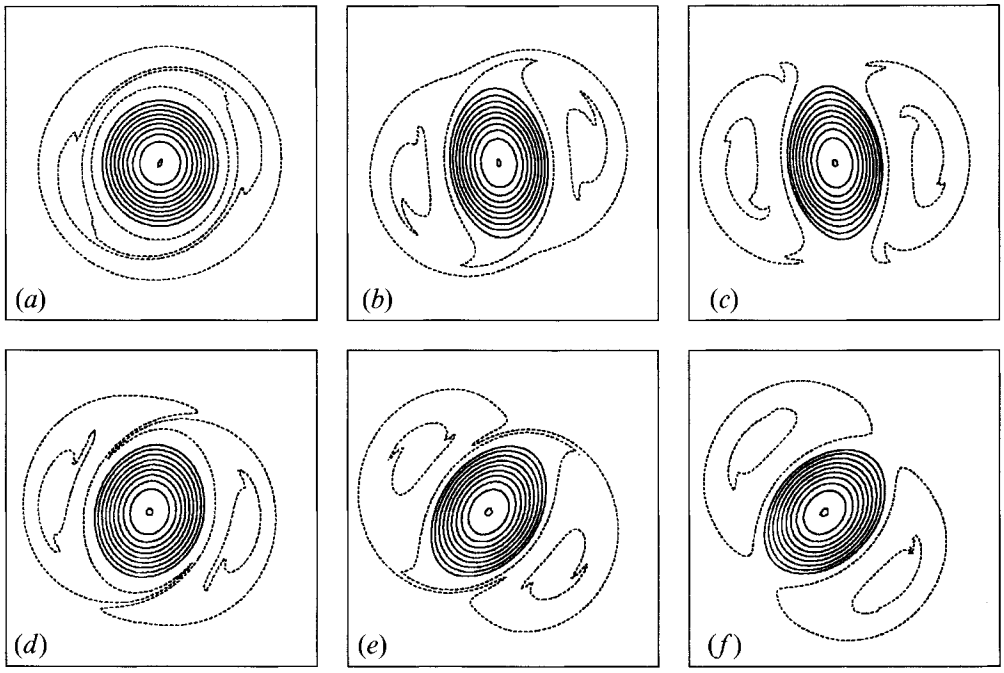

FIGURE 13. Sequence of vorticity maps from a numerical experiment with initial profile $\overline{\zeta}_{2.5}$ at resolution 256^2. (*a*) $t = 40$; (*b*) $t = 80$; (*c*) $t = 120$; (*d*) $t = 160$; (*e*) $t = 200$ and (*f*) $t = 240$. Notice the exchange of filaments at $t = 140$ and bridging between the two satellites at $t = 200$. Contour interval 0.1. Dashed line : negative vorticity. Solid line : positive vorticity.

profile, the mode $\ell = 2$ instability saturates as a stable tripole or splits the vortex into two separating dipoles, as it does for $\alpha \geqslant 3.2$. There is experimental evidence that splitting occurs after the formation of the satellites and that it is due to an instability of the core. More generally, we know that the two satellites only exhibit weak shape vacillations after the generation stage while the core may show strong vacillations, whatever the stability of the tripole.

This leads us to consider a more elaborate model in which the core vortex is replaced by an ellipse of uniform vorticity ω with area A, eccentricity σ and orientation ϕ. The equations for the evolution of the ellipse and the two satellite point vortices can be derived from Legras & Dritschel (1991). If we are only interested in symmetric solutions in solid-body rotation with the point vortices aligned with the minor axis of the ellipse, the equations are

$$\left.\begin{aligned} \dot{\phi} &= \frac{\pi\kappa'}{A}\frac{1-\sigma^4}{\sigma\rho^2} + \frac{\pi\kappa}{2A}(1-\sigma^2)\,, \\ \dot{z}_0 &= \mathrm{i}\frac{\kappa}{\Gamma\overline{\zeta}_0} + \mathrm{i}\frac{\kappa'}{2\overline{z}_0}\,, \\ \dot{z}_0 &= \mathrm{i}z_0\dot{\phi}\,, \end{aligned}\right\} \tag{6.1}$$

where $z_0 = x_0 + \mathrm{i}y_0$ is the complex Cartesian coordinate of one of the satellites, $\kappa = A\omega/2\pi$, $\kappa' = \Gamma_s/2\pi$, $\Gamma = [A\omega/(1-\sigma^2)]^{\frac{1}{2}}$ and $\zeta_0 = \mathrm{i}\rho\mathrm{e}^{\mathrm{i}\phi}$, satisfying $z_0 = \Gamma(\zeta_0 - \sigma\mathrm{e}^{-2\mathrm{i}\phi}\zeta_0^{-1})$, is the location of the satellite in the elliptical coordinate system associated with the ellipse. The additional equation $\dot{\sigma} = 0$ is automatically satisfied when the satellites are aligned along the minor axis of the ellipse. After elementary

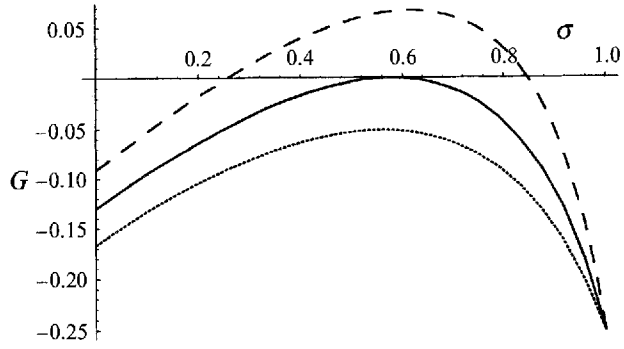

FIGURE 14. Curves $G(\sigma)$ for (dotted) $J = 5$, (solid) $J = 6.7$ and (dashed) $J = 10$.

manipulations, the system (6.1) reduces to

$$G \equiv \sigma\left(\frac{1}{2} - \frac{1}{\rho^2 - \sigma}\right) + A\left(\frac{\sigma}{2(\rho - \sigma/\rho)^2} - \frac{(1+\sigma^2)}{\rho^2}\right) = 0, \tag{6.2}$$

with $A = -\kappa'/\kappa$.

In adddition, the system is characterized by its excess angular momentum

$$\mathscr{I} \equiv 4\pi\kappa'|z_0|^2 + A\kappa\frac{1+\sigma^2}{1-\sigma^2},$$

or

$$J \equiv -\frac{\mathscr{I}}{A\kappa} = 4A\frac{1}{1-\sigma^2}\left(\rho - \frac{\sigma}{\rho}\right)^2 - \frac{1+\sigma^2}{1-\sigma^2}. \tag{6.3}$$

We can determine the equilibrium value σ from A and J by replacing ρ in (6.2) with its expression in (6.3). Figure 14 shows the curves $G(\sigma)$ within the interval [0,1] for $A = \frac{1}{2}$ and different values of J. For $J > J_c = 6.684\ldots$, two solutions exist which correspond respectively to a stable and an unstable fixed-point equilibrium. For $J < J_c$, no solution exists. Using the time-dependent equations, it can be shown that the point-vortex satellites move away while the core elongates indefinitely. This is, within our simple model, the onset of splitting leading to the double dipolar structure.

To sum up these developments, there exists a limited range of situations, depending on the single parameter J for which stationary solutions are possible within the framework of our model. As we did in § 3 for the linear instability we can now fit this model to our continuous profile and define a relation $J(\alpha)$. Using the same argument, we consider that the core vortex is equivalent to a uniform vortex with radius $r = r_1 \equiv (1/\alpha)^{1/\alpha}$ and circulation $\Gamma = 2\pi\int_0^{r_1} r\bar{z}_\alpha(r)\mathrm{d}r$. If we calculate the excess angular momentum of the tripole $\mathscr{I} = 2\pi\int_0^{r_1} r^3\bar{z}_\alpha(r)\mathrm{d}r$, we can define J by

$$J(\alpha) = -\frac{2\mathscr{I}}{r_1^2\Gamma}.$$

It turns out that J is a decreasing function of α and that $J = J_c$ is obtained for $\alpha = 3.178\ldots$, a value which is in perfect agreement with the numerical experiments. It is remarkable that this striking result is obtained in spite of the very crude representation of the satellites by point vortices.

7. Decay of the tripole

7.1. *Description of the asymmetric breaking*

The rotating steady state shown on figure 11 is in fact a metastable stage in the long-term evolution of the unstable shielded vortex. After some time, the oscillations of the perturbation amplitude, which seem damped in the time-series of figure 10, amplify anew, driven by a sharp growth in the mode $\ell = 1$ disturbance. This asymmetry stems from numerical round-off errors in the initial conditions, progressively fed by nonlinear interactions (since mode $\ell = 1$ is linearly stable in a barotropic flow) and vorticity diffusion. The results shown in this section have been obtained with the lower resolution 128^2 and $\nu_4 = 10^{-7}$.

After $t = 18\tau$, this low-resolution experiment exhibits persisting oscillations of the tripole which are accompanied by shedding of positive vorticity from the core vortex each time the tips of the core vortex cross the saddle points. Figure 15 shows a complete cycle of one oscillation. We see that after being released outside of the tripole, and since the total circulation of this latter is zero, the filaments hardly move significantly, nor are they absorbed within the satellite. They are submitted to a strong dissipation which is most effective where the radial section is narrower so that they rapidly reduce to a patch of positive vorticity located where the initial radial profile was broader (see figure 15*c*). They interact again with the core vortex after one half-rotation of this latter (see figure 15*d*). A small part of the patch is then advected along the core edge but the main component joins and reinforces the newly emitted filament (see figure 15*e*, *f*). It is interesting to notice that the oscillations of the core vortex are apparently locked to the rotation period. We conjecture that this is due to the modulation of the external strain by the stripped strands. Indeed, the strain is maximum when the patches return near the main axis of the core vortex thus contributing to maintain the oscillation. The whole process is clearly irreversible since the core vortex is continuously eroded but only a small fraction of its circulation is carried out during one cycle. Hence, the process can repeat many times.

Vorticity diffusion is here instrumental in two respects. First, it permanently regenerates the low-vorticity external layers of the core vortex which are stripped away during each cycle. Without diffusion, a high vorticity gradient tending to infinity would appear on the periphery of the core vortex, adjusting progressively its location in order to confine the core vortex inside the internal separatrices (Legras & Dritschel 1993*b*) and to forbid any further stripping. For finite but small diffusion, such as in our 512^2 experiment with $\nu_8 = 1.5 \times 10^{-18}$, we have seen on figure 8 that the core vortex is indeed bounded by a sharp vorticity gradient. A small amount of diffusion occurs across this gradient but vorticity leakage from the core vortex is considerably reduced with respect to the high-diffusive case of the 128^2 experiment. This is also true to a lesser extent for the intermediate resolution 256^2 with $\nu_4 = 10^{-8}$. In this latter case, we observe that the oscillations of the core vortex are weaker than for the highly diffusive case.

Secondly, it dissipates the filaments and thus makes irreversible the leakage of vorticity from the core vortex towards the exterior of the tripole. Since the excess angular momentum $\int\int \zeta r^2 \mathrm{d}x\,\mathrm{d}y$ must be conserved, this transfer of positive vorticity towards the exterior must be compensated by an outward motion of the two satellites and a slowing down of the rotation period. Both effects are observed: the average angular rotation decreases by 40% between $t = 29\tau$ and $t = 100\tau$ while the distance between the centres of the satellites increases by 30%.

Notice that it has been demonstrated by Swaters (1991) that the viscous (or

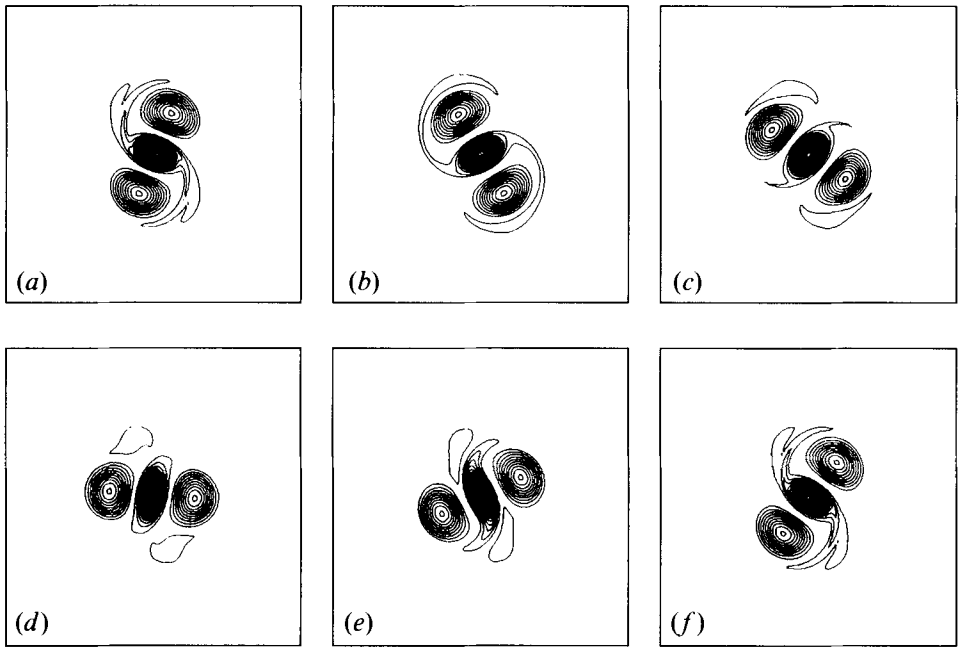

FIGURE 15. Sequence of vorticity maps showing a complete cycle of the tripole oscillation in the lower resolution 128^2 experiment. (*a*) $t = 1200(92.1\tau)$; (*b*) $t = 1240(95.2\tau)$; (*c*) $t = 1260(96.7\tau)$; (*d*) $t = 1280(98.2\tau)$; (*e*) $t = 1300(99.8\tau)$ and (*f*) $t = 1320(101.3\tau)$. Contour interval 0.02.

hyperviscous) decay of a stationary Lamb dipole occurs while maintaining a constant radius. It is reasonable to expect that this result extends to the tripole and thus to consider that the increase of the distance between the satellites and the core vortex only occurs as a consequence of the angular momentum conservation and nonlinear vorticity leakage towards the external region.

The final stage breaks the $\ell = 2$ symmetry so far observed. After $t = 123\tau$ (see figure 16*a*), the core vortex comes slightly closer to one of the satellites. The patches released during the following burst of shedding (see figure 16*b*, *c*) show very distinct asymmetry with a stronger component on the side of the second satellite. Owing to the conservation of vorticity centroid, the core vortex is pushed further towards its closest neighbour. Breaking is completed when the returning main strand is advected back inside the tripole between the core vortex and the second satellite (see figure 16*d*, *e*). Then, a strong pairing occurs between the core vortex and the closest satellite which rapidly move away from the centroid and the second satellite (see figure 16*f*). The subsequent evolution shows the dipole moving on a circle until a new encounter with the now isolated second satellite (see figure 16*g*). During this interaction, the core vortex changes partner and goes away with the second satellite while the first one now stays isolated (see figure 16*h*, *i*). Later on, this cycle repeats itself many times.

Figure 17 summarizes the evolution of the tripole by plotting the perturbation amplitude of mode $\ell = 1$ at time t against its value at time $t - 20$. After the initial instability stage which increases the amplitude to about 0.012, the tripole undergoes a series of 16 cycles during which vorticity leaks from the core vortex to the exterior and the amplitude grows linearly up to 0.02. The linear growth shows that leakage occurs at a constant rate during this period as already suggested by the repetitive

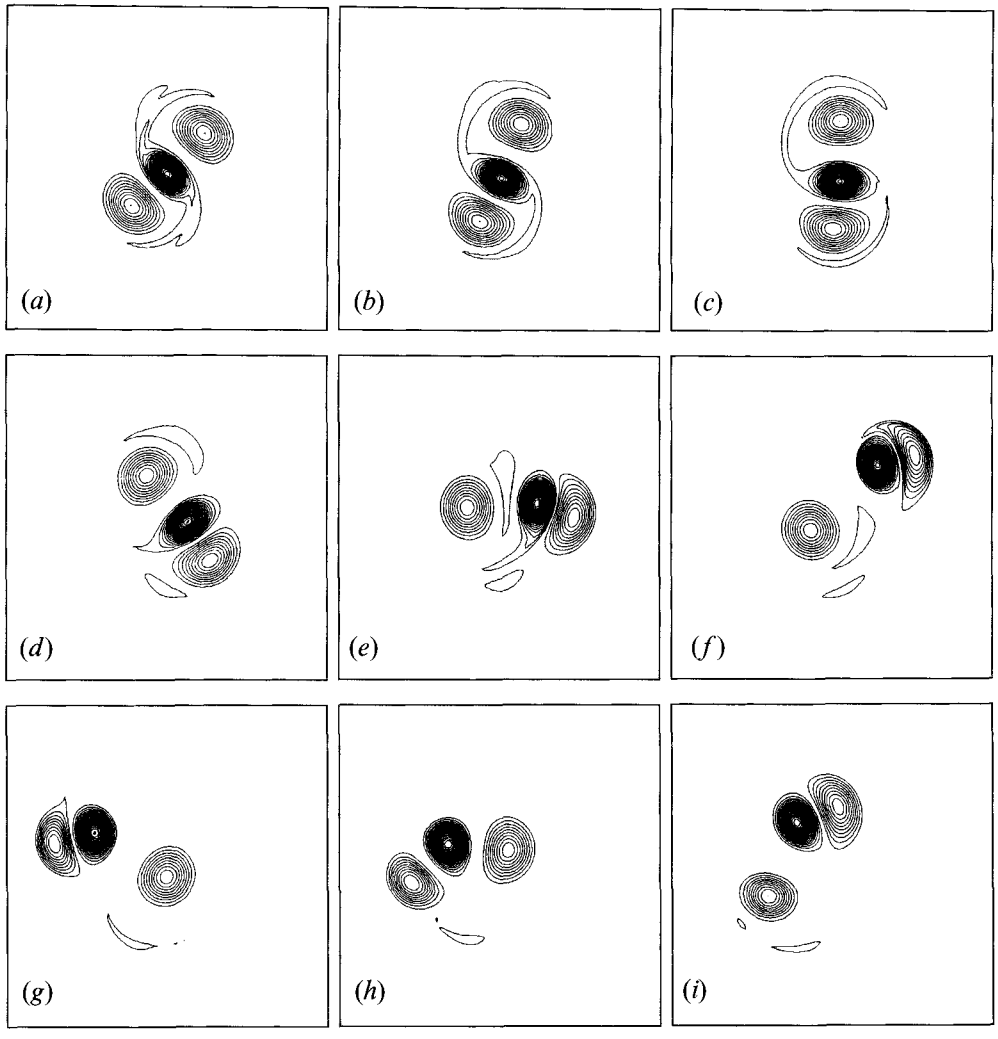

FIGURE 16. Sequence of vorticity maps showing the asymmetric breaking of the tripole in the lower resolution 128^2 experiment. (*a*) $t = 1600(122.8\tau)$; (*b*) $t = 1620(124.3\tau)$; (*c*) $t = 1640(125.9\tau)$; (*d*) $t = 1680(128.9\tau)$; (*e*) $t = 1720(132\tau)$; (*f*) $t = 1760(135.1\tau)$; (*g*) $t = 1960(150.4\tau)$; (*h*) $t = 2000(153.5\tau)$ and (*i*) $t = 2040(156.6\tau)$. Contour interval 0.02.

appearance of the cycle. Then, vortex breaking occurs abruptly and leads to the limit cycle described above with amplitude oscillating around 0.06.

This evolution does not exhibit the character of a plain instability of the tripole with respect to mode $\ell = 1$ perturbation. Clearly, the sudden onset of the instability near $t = 122\tau$ is due to the previous stage of slow convective-diffusive evolution. As the intensity of the core vortex decreases by leakage, the ratio of its circulation to the circulation of one of the satellites decreases in absolute value. In the case of three point vortices, we know from § 6 that the tripole is unstable when this ratio is smaller than 5/4, that is 5/8 times the ratio for a tripole with zero total circulation. We do not know the corresponding threshold for our continuous distribution but it is reasonable to assume that it requires about the same variation of the circulation ratio to pass from the initial tripole to the unstable situation. However, by measuring the

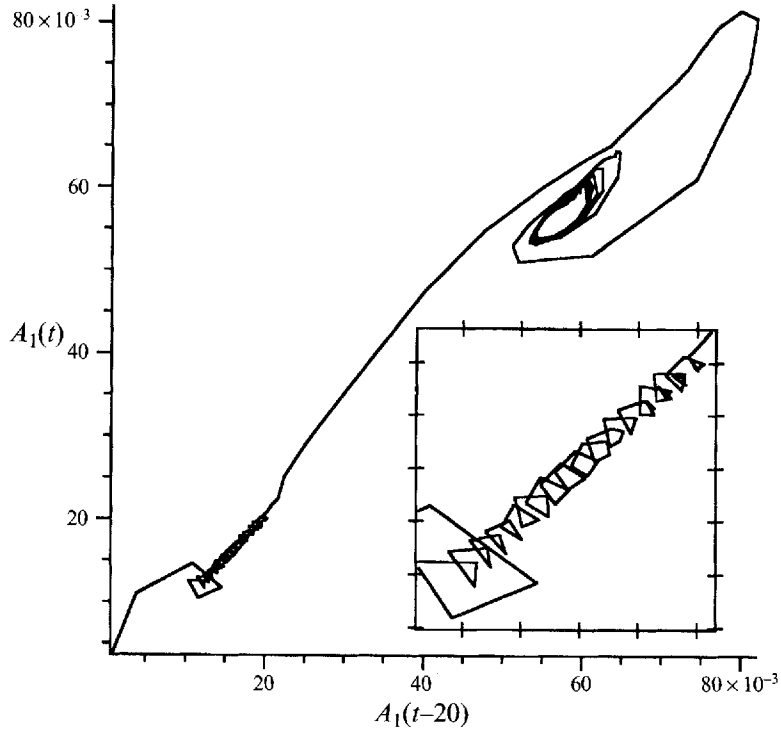

FIGURE 17. Return map of the amplitude $\bar{A}_1$ with a delay $\Delta t = 20$ in the lower resolution 128^2 experiment. The region corresponding to the metastable tripole is enlarged in the insert.

angular rotation Ω and the distance d of the satellites, we find that Ωd^2 decreases by less than 5% between $t = 18\tau$ and $t = 120\tau$. Since, in the meantime, the circulation of the satellite has also decreased, tending to increase the circulation ratio, it is very unlikely that the instability condition gets satisfied.

Indeed, we implicitly assume here that the positive vorticity released outside the vortex does not induce any feedback on the interior motion. This would be true if the distribution was perfectly axisymmetric, which it obviously is not. But the most important effect to be taken into consideration is that the $\ell = 1$ mode of the tripole induces a deformation of the external ring of positive vorticity which can in turn modify the tripole dynamics. The saddle points of the stream function field, which are so important for the erosion of the core vortex, are also able to amplify a non-axisymmetric perturbation. Indeed a small displacement of these points can considerably deviate the trajectory of a vorticity patch passing in their vicinity as seen in figure 16. The simple model described below demonstrates how this effect is able to destabilize the tripole.

7.2. *A modified point-vortex model of asymmetric breaking*

It is fairly difficult to model, even simply, the dynamics of the vorticity ring surrounding the tripole after the erosion of the core vortex. We shall rather adopt here the following ansatz: we treat the asymmetric component of the exterior filaments as belonging to the satellites and we neglect any effect that does not break the symmetry of the tripole. This implies that we do not consider the feedback effect of the exterior ring onto the rotation or onto the symmetric oscillations of the tripole.

Within this framework we can treat the asymmetric component as resulting from an exchange of vorticity between the two satellites when symmetry is broken, the one earning positive vorticity being that which is located to the right of the obtuse angle formed with its partner and the core (for a core with positive circulation). In order to account for this effect, we consider a modified version of the three-point-vortex model introduced in § 3 which takes into account a leakage from one satellite to the other depending on their angle with respect to the central vortex. The equations of motion in complex $z = x + \mathrm{i}y$ coordinates are

$$\left.\begin{aligned} 2\pi\dot{z}_2 &= \frac{\mathrm{i}\Gamma_c}{\bar{z}_2 - \bar{z}_c} + \frac{\mathrm{i}\Gamma_1}{\bar{z}_2 - \bar{z}_1}, \\ 2\pi\dot{z}_1 &= \frac{\mathrm{i}\Gamma_c}{\bar{z}_1 - \bar{z}_c} + \frac{\mathrm{i}\Gamma_2}{\bar{z}_1 - \bar{z}_2}, \\ 2\pi\dot{z}_c &= \frac{\mathrm{i}\Gamma_1}{\bar{z}_c - \bar{z}_1} + \frac{\mathrm{i}\Gamma_2}{\bar{z}_c - \bar{z}_2}, \end{aligned}\right\} \tag{7.1}$$

where z_c, z_1 and z_2 are the locations of the core vortex and the two satellites while Γ_c, Γ_1 and Γ_2 are their circulations. The variation of the circulation of the satellites is described by the following heuristic equation:

$$\ddot{\Gamma}_1 = -\ddot{\Gamma}_2 = -g\frac{\Gamma_c^3}{a^6}\mathrm{Im}[(z_2 - z_c)(\overline{z_1 - z_c})], \tag{7.2}$$

where a is the equilibrium distance between the satellites and the core vortex and g is a governing dimensionless positive parameter controlling the rate of vorticity leakage.

The right-hand side of (7.2) is proportional to the sine of the angle between the satellites and the centre. It models the geometrical dependency of the exchanges described above. The second-order derivative accounts for the delay in a vorticity shred moving away from the saddle point, and thus to convey the effect onto the external strain, after the onset of the asymmetric exchange. Other quantities are for dimensional purposes. We define the dimensionless quantities

$$A = \frac{z_2 + z_1 - 2z_c}{a}\exp\left(-\frac{3\mathrm{i}\Gamma_c t}{8\pi a^2}\right),$$
$$B = \frac{\Gamma_2 - \Gamma_1}{\Gamma_c}, \quad C = \frac{\dot{\Gamma}_2 - \dot{\Gamma}_1}{\Gamma_c},$$

and we linearize the equations with respect to the equilibrium, with $A = A_0 + A'$, $B = B'$ and $C = C'$, yielding

$$\dot{A}' + \mathrm{i}\frac{3}{4}A' = \frac{3}{2}\mathrm{i}B', \quad \dot{B}' = C, \quad \dot{C}' = 2g\mathrm{Im}[A']. \tag{7.3}$$

The characteristic equation of this system (for $A', B', C' \propto \mathrm{e}^{\mu t}$) is

$$\mu(\mu^3 + \tfrac{9}{16}\mu + 3g) = 0. \tag{7.4}$$

This equation has complex roots with positive real parts for $g > 0$. Figure 18 shows, for $g = 0.05$, the evolution of the distance of the two satellites to the core. The alternate pairing of the core with one of the satellites is clearly visible. This simple model demonstrates the mechanism of instability by asymmetric exchanges of vorticity patches across the saddle nodes. Its main weakness lies in the representation of separation delay by a the second-order derivative in (7.2). We have seen that, in reality, instability is observed after a small but finite amount of vorticity has

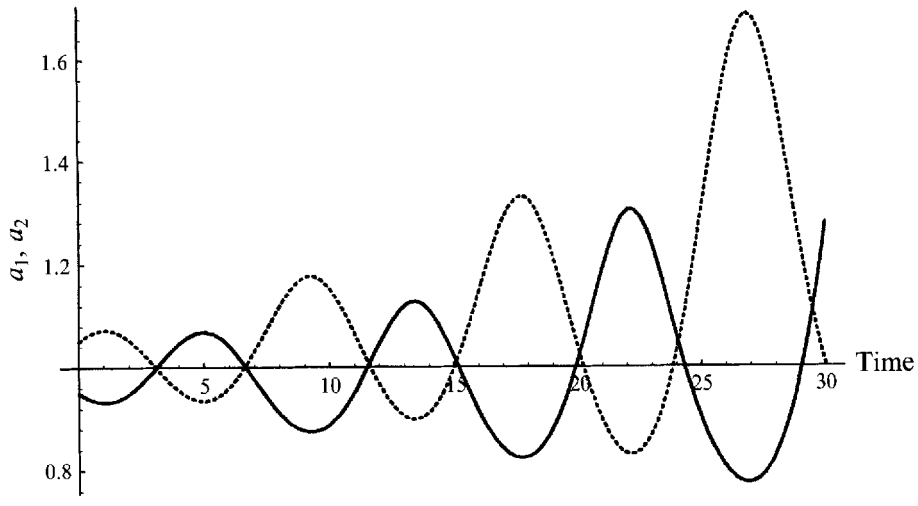

FIGURE 18. Evolution of the distances of the two satellites to the core vortex in the instability of the modified point-vortex model. Solid line : $|a_1(t)|$. Dotted line: $|a_2(t)|$. Initial positions : $a_1(0) = -1 + 0.05(1 + \mathrm{i})$ and $a_2(0) = 1 + 0.05(1 + \mathrm{i})$

been transferred from the core vortex to the exterior of the tripole, which would corresponds to a given value of g in our idealized model. A more quantitative approach would require an explicit representation of the external ring of positive vorticity.

8. Effect of a bottom topography or a free surface

The dynamics so far described does not depend on the sign of the core vortex. The equations are invariant if we invert the sign of the vorticity and velocity and apply a mirror symmetry with respect to, say, the x-axis. This symmetry is broken by adding a bottom axisymmetric parabolic orography $\eta = -\eta_0 r^2$ (the arbitrary constant has been omitted) which is also an idealization of the free surface in a rotating tank. Using the same procedure as above we integrate the equations starting from a vortex with either a cyclonic or an anticyclonic core and with $\eta_0 = 0.1$ (see figure 19). Notice that the initial linear instability is left unchanged by the orography. The nonlinear stage is, however, strongly modified and the resulting flow differs between the two cases.

Figure 19(a) shows that a cyclonic core still yields a tripole according to the scenario detailed in previous sections. The main differences are a longer linear phase and a more compact final distribution, where the satellites get closer to the core than they do in the absence of orography. The tumbling of the core is also reduced at the end of the saturation stage.

Figure 19(b) shows that starting from an anticyclonic core leads to a very different situation in which the nonlinear amplification is able to tear the core vortex to a point where it breaks in two parts. These two parts then form two pairs with the satellites of opposite sign and move away (see figure 19c).

These effects are due to the vertical stretching or compressing of the vorticity tubes entrained within the two satellites. The outward motion of the vorticity contained within the two satellites is accompanied by reinforcement when it is positive (for

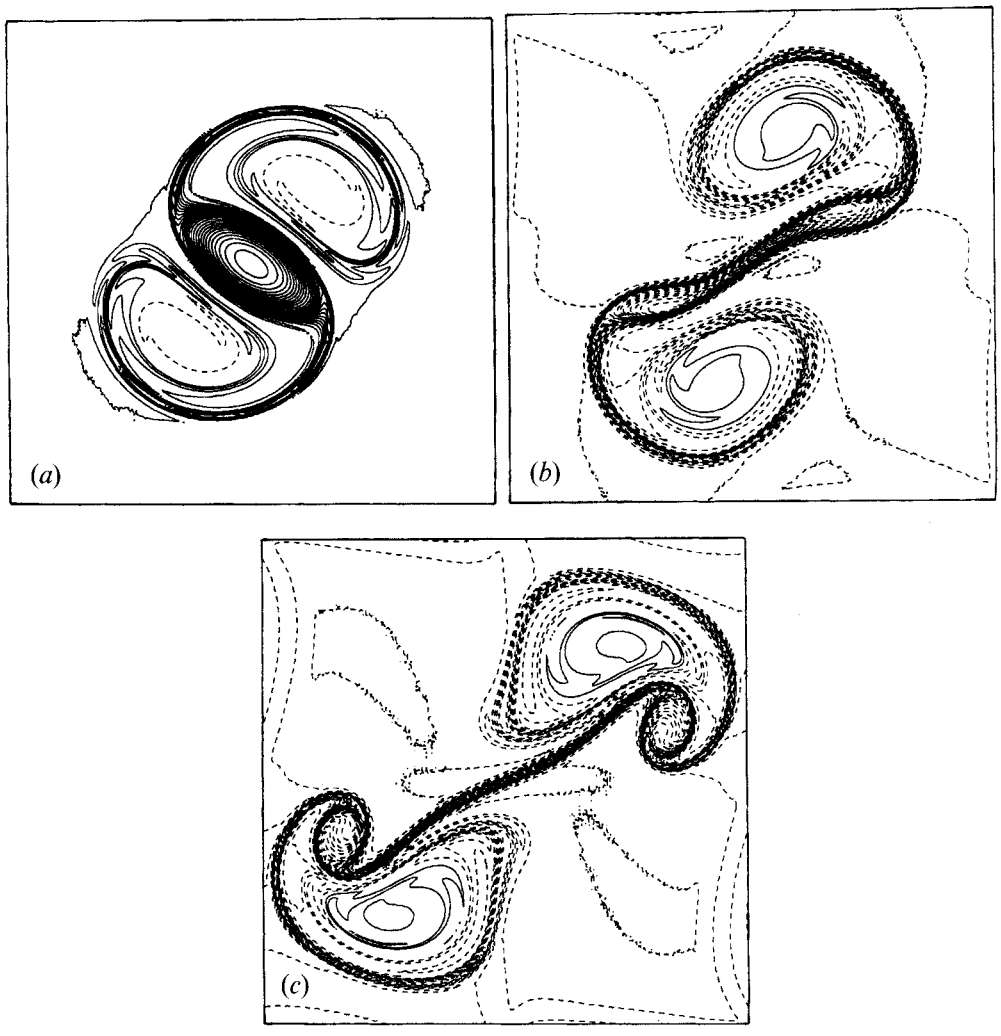

FIGURE 19. Vorticity maps of the two experiments with orography. (*a*) Cyclonic core and $t = 105(8.06\tau)$; (*b*) anticyclonic core and $t = 105$; (*c*) anticyclonic core and $t = 120$. Contour interval 0.05.

the anticyclonic core) and by weakening when it is negative (for the cyclonic core). The strain felt by the core vortex is thus intensified or reduced depending on the core polarity. In the anticyclonic case breaking may ensue, while in the cyclonic case saturation is easier to obtain and the tripole is stabilized. Similar effects were studied by Carnevale, Kloosterziel & van Heijst (1991).

The experiment of Kloosterziel & van Heijst (1991) was performed in a rotating tank with a free surface. These authors found that a tripole could be easily generated with an initial cyclonic core, while with an anticyclonic core the vortex broke into two dipoles moving apart. This asymmetry does not seem, however, due to the free surface effect. Using their parameters and velocity measurements, we find $\zeta \approx 6.6(1 - r^2/2)\exp(-r^2/2)$ and $\eta_0 = 0.001r^2$. The free surface effect is thus two orders of magnitude less than in our numerical experiment, that is much too weak to account for the observed asymmetry. As already noticed by Kloosterziel & van

Heijst, the sensitivity of anticyclones to three-dimensional instabilities is more likely to explain the cyclonic preference in their case. It is, however, striking that the final stage of their experiment with an initial anticyclonic core, shown in their figure 5(c, d), is very similar to our figure 19(b, c). As a tentative explanation, we may conjecture that the three-dimensional instability does not destroy completely the two-dimensional vortex but homogenizes its anticyclonic core. This situation brings the vortex towards a profile with steeper vorticity gradient or, equivalently, larger value of α which exhibits dipolar breaking.

Finally, we list a series of observations made on the long timescale while varying only η_0 within the initial conditions and integrating up to $t = 70\tau$. Here C and AC respectively denote the cases with cyclonic or anticyclonic core vortices.

(i) If $\eta_0 = 0.005$ (resp. 0.02), C forms a tripole, strongly filaments and exhibits a slow growth of the disturbance with time, but does not break. AC also filaments and asymmetrically breaks at $t = 60\tau$ (resp. 50τ).

(ii) If $\eta_0 = 0.25$, C forms a tripole, which strongly oscillates and filaments, before asymmetric breaking at $t = 60\tau$. The final state shows five alternate poles on the same axis.

(iii) If $\eta_0 = 0.5$, the core vortex of C breaks at $t = 8\tau$, and forms an inverted tripole after merging of the former satellites. The new satellites eventually merge to yield an asymmetric rotating dipole.

(iv) Finally, if $\eta_0 = 0.75$, the core vortex of C breaks at $t = 8\tau$. The two fragments do not immediately withdraw from the centre; they keep a figure-eight shape, and a transient quadrupole is formed. An inverted tripole is formed at $t = 33\tau$.

Cyclones are therefore much more prone to form tripoles (direct or inverse) in the presence of a bottom relief than anticyclones which produce dipoles. The development of asymmetric instabilities from the interaction with topography has been recently observed in a rotating tank and modelled by G.J.F. van Heijst & O.U. Velasco-Fuentes (1993, personal communication).

9. Conclusions

The tripoles are now well-known features of two-dimensional vortex flows (the first observations date back to 1988). This study sheds new light on their generation from unstable shielded monopoles and on their decay in weakly dissipative conditions. One of the main reason to study such, apparently exotic, structures is that they reveal many of the basic mechanisms of vortex dynamics.

The first stage of the development of the small-amplitude perturbation is well described by the linear theory. The instability of our family of continuous profile has been related to the properties of a more general family of piecewise uniform profiles with two parameters.

Two stages of nonlinear amplification and saturation follow. An attempt was made by Carton (1988) to derive an amplitude equation in the inviscid case. It turned out that a Landau equation could not be obtained at third order of the expansion, as is usually the case, but required a fourth-order expansion which has not been performed. This difficulty could be related with the high level of nonlinearity of the saturation stage involving stripping of vorticity from the core vortex and wrapping of the resulting shreds around the satellites. Instead, we find here that a simple model based on the interaction between one ellipse and two point vortices is able to account for the saturation of the initial instability. The key parameter is the total angular

momentum of the vortex which must be large enough to allow the existence of the tripole.

The stripping of vorticity filaments from the core vortex is easily interpreted by the existence of saddle points of the corotating stream function. A noticeable consequence is the generation of high vorticity gradients on the periphery of the core vortex. These saddle points are also involved in the decaying stage of the tripole: they maintain the sharp boundary of the core vortex and convey the vorticity leaking across it to the exterior of the tripole, the total leakage being controlled by the value of diffusion. The progressive reinforcement of the exterior ring leads to a situation where the tripole is unstable to perturbations breaking the symmetry with respect to the origin. This instability leads to an oscillatory behaviour with one dipole on one side and an isolated monopole on the other side, which periodically collide and exchange partners. This final stage is qualitatively analysed using a modified point-vortex model allowing transfers of vorticity between the satellites.

This study also demonstrates the good correlation between numerical and laboratory experiments, as both have been historically simultaneous. For instance, asymmetric breaking is equally observed in rotating-tank experiments, by excitation of mode $\ell = 1$ with a parabolic free surface. A quantitative interpretation of the laboratory experiment is, however, made difficult by the absence of accurate data on the aisle of the velocity profile which is so important in determining the properties of the instability.

In the presence of a moderate topographic effect, the saturation stage is strongly modified leading to the stabilization of tripoles with cyclonic cores and to the destabilization of tripoles with anticyclonic cores. We have just touched on the influence of strong topographic effects which seems to offer a large variety of phenomena. Notice, however, that the topographic effect is not sufficient to reproduce the experimental free-surface influence. Other mechanisms such as three-dimensional ageostrophic movements or boundary layer effects should be investigated. Bottom topography plays an essential role in the dynamics of real ocean vortices and is worth a complete investigation. Indeed, the only available observation of a tripole has been obtained in the Bay of Biscay (Pingree & LeCann 1992) as a result of the encounter of a coastal current with a trough and a cape.

Finally, one may wonder about the existence of higher-order multipolar structures beyond the tripole in two-dimensional incompressible flows. It has been recently established that one is very unlikely to observe long-lived structures which are more complex than quadrupoles (Carnevale & Kloosterziel 1994; Morel & Carton 1994).

It would be gratifying and profitable to find more occurrences of such structures in geophysical vortex flows. This raises the question of the free-decay assumption on which this study lies. Since tripoles have also been observed in forced two-dimensional turbulence and are known to exist as stationary solutions within a large-scale uniform strain (A. Dobritsyn, personal communication), their resistance to a stochastic mechanical forcing or to varying large-scale deformation fields (such as the planetary vorticity gradient or the influence of neighbouring intense currents) should be tested.

Discussions with G.R. Flierl, J.C. McWilliams and G.J.F. van Heijst proved timely and valuable. The first author's financial and computational support was provided by the Service Hydrographique & Océanographique de la Marine under the PAMIR

research programme. The Centre de Calcul Vectoriel pour la Recherche has provided the computer resources used for high-resolution experiments.

Appendix A. Stability of a uniform vorticity tripole

We consider the uniform vorticity profile described in § 3. We take here $c = 1$ without losing generality. The radial velocity profile $V(r)$ is given by

$$\left.\begin{array}{ll} 0 < r < a & V(r) = \dfrac{r}{2}, \\ a < r < b & V(r) = \dfrac{a^2}{2r}, \\ b < r < 1 & V(r) = \dfrac{a^2}{2(1-b^2)}\left(\dfrac{1}{r} - r\right), \\ 1 < r & V(r) = 0. \end{array}\right\} \tag{A 1}$$

Assuming a perturbation stream function $\mathrm{Re}[\varphi(r)\exp(\mathrm{i}\ell(\theta - \hat{c}t))]$ with azimuthal wavenumber ℓ and angular phase speed $\hat{c}$, the Rayleigh equation is:

$$(r\hat{c} - V)\left(\frac{\mathrm{d}^2\varphi}{\mathrm{d}r^2} + \frac{1}{r}\frac{\mathrm{d}\varphi}{\mathrm{d}r} - \frac{\ell^2}{r^2}\varphi\right) + \varphi\frac{\mathrm{d}Q}{\mathrm{d}r} = 0, \tag{A 2}$$

where $Q(r)$ is the piecewise uniform basic vorticity profile. Its solution is given here by

$$\begin{array}{ll} 0 < r < a & \varphi(r) = a_1 r^{\ell}, \\ a < r < b & \varphi(r) = a_2 r^{\ell} + b_2 r^{-\ell}, \\ b < r < 1 & \varphi(r) = a_3 r^{\ell} + b_3 r^{-\ell}, \\ 1 < r & \varphi(r) = b_4 r^{-\ell}, \end{array}$$

where the constants a_i, b_i are obtained by letting ϕ be continuous over $0 < r < \infty$ and integrating (A 2) across the discontinuities of $Q(r)$. We get the following set of relations :

$$\begin{aligned} a^{2\ell}a_1 &= a^{2\ell}a_2 + b_2, \\ b^{2\ell}a_2 + b_2 &= b^{2\ell}a_3 + b_3, \\ a_3 + b_3 &= b_4, \\ \ell(\tfrac{1}{2} - \hat{c})(a^{2\ell}(a_2 - a_1) - b_2) &= -a^{2\ell}a_1, \\ \ell\left(\frac{a^2}{2b^2} - \hat{c}\right)(b^{2\ell}(a_3 - a_2) + b_2 - b_3) &= -q(b^{2\ell}a_3 + b_3), \\ -\ell\hat{c}(b_4 - b_3 + a_3) &= -qb_4. \end{aligned}$$

In order to admit non-trivial solutions, the determinant of the above system must vanish, yielding a dispersion relation for $\hat{c}$. When $\ell = 2$ and after some algebraic manipulations, we obtain

$$64b^4\hat{c}^3 - 16b^2(2a^2 + b^2)\hat{c}^2 + 4a^2(2b^2 - a^4(1 + b^2) + a^2b^2(2 + b^2))\hat{c} + a^8 - a^4b^2(b^2 + 2) = 0, \tag{A 3}$$

which is solved numerically. The resulting stability diagram is shown on figure 3.

Appendix B. Interior and exterior strain

In order to separate the two components of the strain, we first notice that vorticity contours remain quasi-elliptical within the core region, as can be easily checked from

figure 1. We also observe that the ellipses stay aligned and that the eccentricity σ varies weakly within the core. Under these conditions, it can be shown (Legras & Dritschel 1991) that the internal component of the strain at the centre of the core is $\gamma_i = \frac{1}{2}\sigma\omega_0$ where ω_0 is the vorticity at the centre. If, in addition, we know the orientation ϕ_i of the core, the amplitude γ_e and the orientation ϕ_e of the external strain can be obtained by solving

$$\gamma_e \sin 2\phi_e = \frac{\partial^2\psi}{\partial x \partial y}(0) - \gamma_i \sin 2\phi_i \,, \tag{B 1}$$

$$\gamma_e \cos 2\phi_e = \frac{1}{2}\left(\frac{\partial^2\psi}{\partial x^2}(0) - \frac{\partial^2\psi}{\partial y^2}(0)\right) - \gamma_i \cos 2\phi_i \,. \tag{B 2}$$

In practice σ and ϕ_i are computed from the moments $M_{mn} = \int\int_D x^m y^n \mathrm{d}x\mathrm{d}y$ of the domain D enclosed by the vorticity contour $\omega = 0.6$. We have

$$\sigma = \frac{\left[4M_{11}^2 + (M_{20} + M_{02})^2\right]^{\frac{1}{2}}}{M_{20} + M_{02} - 2\left[M_{20}M_{02} - M_{11}^2\right]^{\frac{1}{2}}} \,,$$

and

$$\tan 2\phi_i = 2M_{11}/(M_{20} - M_{02}) \,.$$

REFERENCES

Basdevant, C., Legras, B., Sadourny, R. & Beland, M. 1981 A study of barotropic model flows: intermittency, waves and predictability. *J. Atmos. Sci.* **38**, 2305–2326.

Beigie, D., Leonard, A. & Wiggins, S. 1992 The dynamics associated with the chaotic tangles of two-dimensional quasiperiodic vector fields : theory and applications. In *Nonlinear Phenomena in Atmospheric and Oceanic Sciences* (ed. G. Carnevale & R. Pierrehumbert), pp. 47–138. Springer.

Carnevale, G. F. & Kloosterziel, R. C. 1994 Emergence and evolution of triangular vortices. *J. Fluid Mech.* **259**, 305–331.

Carnevale, G. F., Kloosterziel, R. C. & Heijst, G. J. F. van 1991 Propagation of barotropic vortices over topography in a rotating tank. *J. Fluid Mech.* **233**, 119–139.

Carton, X. 1988 Stabilité des structures cohérentes mono- et multipolaires dans les écoulements bidimensionnels et quasi-géostrophiques bi-couches. PhD thesis, Université P. and M. Curie.

Carton, X., Flierl, G. R. & Polvani, L. 1989 The generation of tripoles from unstable axisymmetric isolated vortex structures. *Europhys. Lett.* **9**, 339–344.

Flierl, G. R. 1988 On the instability of geostrophic vortices. *J. Fluid Mech.* **197**, 349–388.

Gent, P. R. & McWilliams, J. C. 1986 The instability of barotropic circular vortices. *Geophys. Astrophys. Fluid Dyn.* **35**, 209–233.

Heijst, G. J. F. van, Kloosterziel, R. C. & Williams, C. W. M. 1991 Laboratory experiments on the tripolar vortex in a rotating fluid. *J. Fluid Mech.* **225**, 301–331.

Hoskins, B. J., McIntyre, M. E. & Robertson, A. W. 1985 On the use and significance of isentropic potential vorticity maps. *Q. J. R. Met. Soc.* **111**, 877–946.

Kida, S. 1981 Motion of an elliptic vortex in a uniform shear flow. *J. Phys. Soc. Japan* **50**, 3517–3520.

Kloosterziel, R. C & Heijst, G. J. F. van 1991 An experimental study of unstable barotropic vortices in a rotating fluid. *J. Fluid Mech.* **223**, 1–24.

Legras, B. & Dritschel, D. G. 1993*a* A comparison of the contour surgery and pseudo-spectral methods. *J. Comput. Phys.* **104**, 287–302.

Legras, B. & Dritschel, D. G. 1993*b* Vortex stripping and the generation of high vorticity gradients in two-dimensional flows. *Appl. Sci. Res.* **51**, 445–455.

Legras, B. & Dritschel, D. G. 1991 The elliptical model of two-dimensional vortex dynamics. Part I : The basic state. *Phys. Fluids* A **3**, 845–854.

LEGRAS, B., SANTANGELO, P. & BENZI, R. 1988 High-resolution numerical experiments for forced two-dimensional turbulence. *Europhys. Lett.* **5**, 37–42.

MCWILLIAMS, J.C. 1984 The emergence of isolated coherent vortices in turbulent flow. *J. Fluid Mech.* **146**, 21–43.

MONTGOMERY, D. & JOYCE, G. 1974 Statistical mechanics of negative temperature states. *Phys. Fluids* **17**, 1139–1145.

MOREL, Y. & CARTON, X. 1994 Multipolar vortices in two-dimensional incompressible flows. *J. Fluid Mech.* **267**, 23–51.

ORLANDI, P. & HEIJST, G.J.F. VAN 1992 Numerical simulations of tripolar vortices in 2d flow. *Fluid Dyn. Res.* **9**, 179–206.

PINGREE, R. & LE CANN, B. 1992 Three anticyclonic slope water oceanic eddies (SWODDIES) in the Southern Bay of Biscay in 1990. *Deep-Sea Res.* **39**, 1147–1175.

POLVANI, L. & CARTON, X. 1990 The tripole: a new coherent vortex structure of incompressible two-dimensional flows. *Geophys. Astrophys. Fluid Dyn.* **51**, 87–102.

ROBERT, R. & SOMMERIA, J. 1991 Statistical equilibrium states for two-dimensional flows. *J. Fluid Mech.* **229**, 291–310.

SWATERS, G.E. 1991 Dynamical characteristics of decaying Lamb couples. *Z. Angew. Math. Phys.* **42**, 109–121.

TAVANTZIS, J. & TING, L. 1988 The dynamics of three vortices revisited. *Phys. Fluids* **6**, 1392–1409.